Dynamic Modeling and Thermal Characterization of Lithium-Ion Batteries

by

Khaled I. Alsharif

Submitted in Partial Fulfillment of the Requirements

for the Degree of

Master of Science in Engineering

in

Electrical Engineering

YOUNGSTOWN STATE UNIVERSITY

May 2023

Dynamic Modeling and Thermal Characterization of Lithium-Ion Batteries

Khaled I. Alsharif

I hereby release this **thesis** to the public. I understand that this **thesis** will be made available from the OhioLINK ETD Center and the Maag Library Circulation Desk for public access. I also authorize the University or other individuals to make copies of this thesis as needed for scholarly research.

Signature:

_____

Khaled I. Alsharif, Student Date

Approvals:

_____

Kyosung Choo, PhD, Thesis Advisor Date

_____

Frank X. Li, PhD, Committee Member Date

_____

Alexander H. Pesch, Dr. Eng., Committee Member Date

_____

Salvatore A. Sanders, PhD, Dean, College of Graduate Studies Date

Abstract

Lithium-ion batteries have revolutionized our everyday lives by laying the foundation for a wireless, interconnected and fossil-fuel-free society. Additionally, the demand for Li-ion batteries has seen a dramatic increase, as the automotive industry shifts up a gear in its transition to electric vehicles.

To optimize the power and energy that can be delivered by a battery, it is necessary to predict the behavior of the cell under different loading conditions. However, electrochemical cells are complicated energy storage systems with nonlinear voltage dynamics. There is a need for accurate dynamic modeling of the battery system to predict behavior over time when discharging. The study conducted in this work develops an intuitive model for electrochemical cells based on a mechanical analogy. The mechanical analogy is based on a three degree of freedom spring-mass-damper system which is decomposed into modal coordinates that represent the overall discharge as well as the mass transport and the double layer effect of the electrochemical cell. The dynamic system is used to estimate the cells terminal voltage, open-circuit voltage and the mass transfer and boundary layer effects. The modal parameters are determined by minimizing the error between the experimental and simulated time responses. Also, these

estimated parameters are coupled with a thermal model to predict the temperature profiles of the lithium-ion batteries. To capture the dynamic voltage and temperature responses, hybrid pulse power characterization (HPPC) tests are conducted with added thermocouples to measure temperature. The coupled model estimated the voltage and temperature responses at various discharge rates within 2.15% and 0.40% standard deviation of the error.

Additionally, to validate the functionality of the developed dynamic battery model in a real system, a battery pack is constructed and integrated with a brushless DC motor (BLDC) and a load. Moreover, because of the unique pole orientation that a BLDC motor possesses, it puts a pulsing dynamic load on the battery pack of the system. HPPC testing was conducted on the cell that is used in the battery pack to calibrate the model parameters. After the battery model is calibrated, the rotation experiment is conducted at which a battery pack is used to drive a benchtop BLDC motor with a magnetorheological brake as a programable load at varying running speeds. The voltage and current of the battery and the BLDC motor driver are recorded. Meanwhile, the speed and the torque of the motor are recorded. These data are compared to the predicted voltage of the battery pack using the mechanical analogy model. The model estimated the voltage response of a battery pack within 0.0385% standard deviation of the error.

Acknowledgements

First, I would like to thank Allah for the blessings that he has given me throughout my life to get me to this point. Without his guidance, none of my success would be possible; therefore, I owe it all to him.

Second, I would like to thank my family, especially my parents, for the core values that they have embedded in me ever since my youth. Their continuous support played a major role in getting me to this point.

Third, I would like to dedicate a special thank you to my fiancé, Nisreen Shuman. She has been nothing but the best support system that anyone can ask for and my best friend throughout this journey. I love you, my queen.

Fourth, I would like to thank my advisor, Dr. Kyosung Choo. Thank you for being the best mentor and teacher that anyone could ask for.

Fifth, I would like to thank Dr. Alex Pesch for being a friend when I needed one and an academic mentor when I needed one.

Lastly, I would like to thank Dr. Frank Li, Dr. Pedro Cortes, and Dr. Vamsi Borra for supporting my research activities and providing me with the resources needed to complete my thesis.

Additionally, I would like to acknowledge the ADMETE program for funding my master's studies.

Publications

1. **K.I. Alsharif**, A.H. Pesch, V. Borra, F.X. Li, P. Cortes, E. Macdonald and K. Choo, "A Coupled Thermo-Mechanical Dynamic Characterization of Cylindrical Batteries," IEEE *Access*, 2022, (10) 51708 - 51722. DOI: 10.1109/ACCESS.2022.3173640.
2. **K.I. Alsharif**, A.H. Pesch, V. Borra, F.X. Li, P. Cortes, E. Macdonald and K. Choo, "A Novel Modal Representation of Battery Dynamics," IEEE *Access*, 2022, (10) 16793-16806. DOI: 10.1109/ACCESS.2022.3149617.
3. **K.I Alsharif**, A. Glaspell and K. Choo, "Energy Conservation Measures for a Research Data Center in an Academic Campus," Energies, 2021, (14) 10-2820. DOI: 10.3390/en14102820.
4. **K.I. Alsharif**, A.H. Pesch, V. Borra, F.X. Li, P. Cortes, E. Macdonald and K. Choo, "Transient Thermal and Electrical Characteristics of a Cylindrical $LiFeS_2$ Cell with Equivalent Circuit Model," *International Conference of Fluid Flow, Heat and Mass Transfer*, Jun 8-10, 2022, Niagara Falls, Canada.
5. **K.I. Alsharif**, A.H. Pesch, V. Borra, F.X. Li, P. Cortes and K. Choo, "Development of a Battery Model for BLDC Motor Applications," SAE Energy & Mobility Technology, Systems and Value Chain Conference & Expo. Under Review.

Table of Contents

List of Figures

List of Tables

Chapter 1 Introduction

A battery is an electrochemical device used to store energy. Electrochemical cells are becoming increasingly important in the industry and everyday life [1], [2]. To optimize the power and energy that can be delivered by a battery, it is necessary to predict the behavior of the cell under different loading conditions. However, electrochemical cells are complicated dynamic systems with time-varying current and voltage output. Additionally, lithium-ion (Li-ion) batteries have been extensively utilized as a major source of power in various energy storage applications due to their high energy density, light weight, long lifespan, charge efficiency, minimal memory effect and design flexibility [3]. Therefore, to predict and optimize the usage of cells, modern engineering requires intuitive dynamic models that accurately describe the input and output relationship. This chapter introduces the fundamental of Li-ion batteries, discusses the energy storage applications that Li-ion batteries are used in, highlights the main contribution of the study conducted in this thesis, outlines the organization of the thesis and finally the chapter is concluded with closing remarks.

1.1. Lithium-Ion Batteries

This section introduces the foundation of Li-ion batteries. First, a brief history of the development of Li-ion batteries is presented. Second, the assembly and operation of an electrochemical Li-ion cell is discussed. Third, the basic terminology utilized with regards to batteries are presented. Forth, different cell configurations and chemistries utilized to construct Li-ion batteries are illustrated and compared. Lastly, typical charge and discharge curves are exemplified and deliberated.

1.1.1. Brief History & Advancements

Lithium-ion batteries have revolutionized our everyday lives by laying the foundation for a wireless, interconnected and fossil-fuel-free society. It started in 1817, when Anfwedson and Berzelius discovered lithium by analyzing petalite ($LiAlSi_4O_{10}$); however, it was not till late the 1960s that non-aqueous 3V Li-ion batteries were available on the market [4]. Table 1.1 illustrates the earlier patents published that led to the development of the current state-of-art Li-ion battery technology [4]. In 1991, Sony Co. introduced Li-ion batteries in digital camcorders, followed by, a widespread of personal electronics such mobile phones, laptops, digital cameras, and power tools utilize Li-ion batteries as their power source [5]. Additionally, as the automotive industry shifts up a gear in its transition to electric vehicles, the demand for Li-ion batteries has seen a dramatic increase. According to [6], the of global Li-ion battery demand in electric vehicles is estimated to see a

77.78%, 89.23% and 92.57% increase in the U.S.A, Europe and China by 2030, respectively. Additionally, the global Li-ion battery market is projected to increase by 55.55% in 2026 [6].

Table 1.1: Li-ion battery earlier patents

Inventor	Company	Title	Number	Date
M. Armand & M. Duclot	AVAR, France	See [4]	French 7,832,976	Nov. 1978
J.B. Goodenough & K. Mizushima	UK Atomic Energy	Fast ion conductors	U.S. 4,357,215A	Apr. 1979
J.B. Goodenough & K. Mizushima	UK Atomic Energy	Electrochemical cell with fast ion conductor	U.S. 4,302,518	Mar. 1980
S. Basu	Bell Labs Inc.	Graphite/Li molten salt	U.S. 4,304,825	Nov. 1980
M. Armand & M. Duclot	AVAR, France	See [4]	U.S. 4,303,748	Jan. 1981
H. Ikeda, K. Narukawa & H.Nakashima	Sanyo Co.	Graphite/Li in nonaqueous solvents	Japanese 1,769,661	Jun. 1981
S. Basu	Bell Labs Inc.	Graphite/Li in nonaqueous solvents	U.S. 4,423,125A	Sep. 1982
Yoshino, K. Jitsuchika & T. Nakajima	Asahi Chemical Ind.	Li-ion battery based on carbonaceous material	Japanese 1,989,293	Oct. 1985
N. Nishi, H. Azuma & A. Omaru	Sony Co.	Non-aqueous electrolyte cell	U.S. 4,959,281	Aug. 1989
M. Fujimoto, N. Yoshinaga & K. Ueno	-	Li-ion secondary batteries	Japanese 3,229,635	Nov. 1991

Shown in Figure 1.1 (*a*) are the energy demand trajectories on Li-ion batteries in the U.S.A., Europe and China from 2019 to 2030. Moreover, Figure 1.1 (*b*) is the projections of the global market revenue for Li-ion batteries from 2020 to 2026.

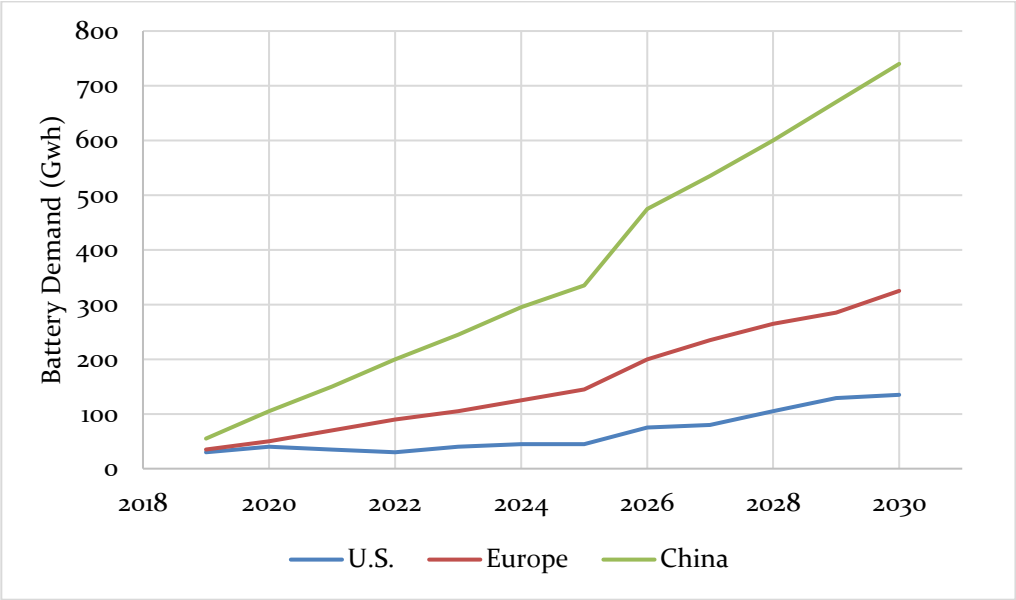

(a)

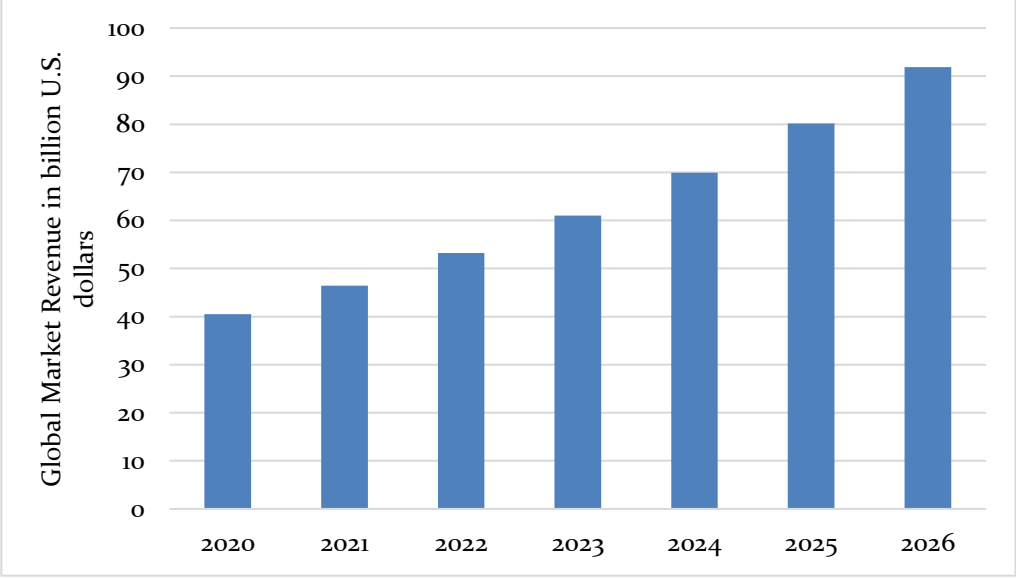

(b)

Figure 1.1: Li-ion battery trajectories

1.1.2. Fundamentals

A typical Li-ion battery consists of a negative electrode known as the anode, a positive electrode known as the cathode, the electrolyte and a separator as illustrated in Figure 1.2 [7].

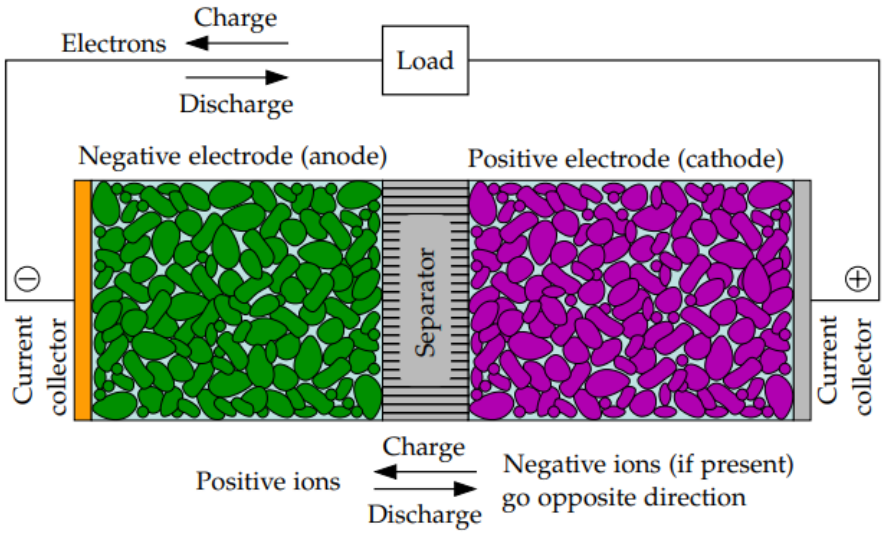

Figure 1.2 : Lithium-Ion battery assembly and operation

During charge, the electrons flow into the anode from the external circuit, Additionally, Li-ions flow from the cathode to the anode. This process causes a redox reaction at the anode and an oxidation reaction at the cathode. Similarly, during discharge, the electrons flow from the anode into the external circuit and cathode accepts Li-ions from the anode, which causes a redox reaction and an oxidation reaction at the anode. The chemical formulation is shown through (1.1) – (1.2) at the cathode and anode for a Li-ion Phosphate cell.

$$Li_{1-x}FePO_4 + xLi^+ + xe^- \underset{charge}{\overset{discharge}{\rightleftharpoons}} LiFePO_4 \quad (1.1)$$

$$Li \underset{charge}{\overset{discharge}{\rightleftharpoons}} Li^+ + e^- \quad (1.2)$$

Additionally, the electrolyte is the ionic conductor that provides a medium for the internal ionic charge transfer between the electrodes. Moreover, the separator functions as an ionic conductor but an electronic insulator to prevent an internal short-circuit between the electrodes from occurring. Lastly, the current collectors, adhere to the electrodes and act as positive and negative terminals to the cell [8].

1.1.3. Basic Battery Terminology

To gain a better understanding of the study conducted in this thesis, below is a list of some basic terminology used with regards to batteries [8], [9]:

- Nominal capacity: The quantity of electric charge which can be stored during charge and released during discharged. Capacity is expressed in coulombs (C) or ampere-hours (Ah).
- C-rate: The rate at which the battery is charged or discharged. For instance, if a 20 Ah battery is being discharged at 20 A, then the discharge rate is 1C; therefore, the battery is expected to fully discharge within an hour. However, if the battery is being discharged at 10 A, then the discharge rate corresponds to C/2 and the battery will fully discharge in 2 hours.

- Open-Circuit Voltage: The voltage across battery terminals when the cell is unloaded and in equilibrium.
- Energy capacity: The amount of electrical energy in watts hours (Wh), computed by multiplying the cell's nominal voltage by its nominal capacity.
- Specific Energy and Energy density: Measures of the maximum amount of energy stored per unit weight or volume. For a given weight, a higher specific energy cell will store more energy. Moreover, for a given volume, a higher energy density cell chemistry will store more energy.
- State-of-Charge (SOC): The ratio of the available capacity to the maximum possible charge that can be stored in a battery.
- Depth-of-Discharge (DoD): The percentage of the battery that has been discharged relative to the overall capacity of the battery.
- Voltage limits: The maximum and minimum allowable voltage thresholds that the battery can operate within. Charging or discharging outside this range is possible but may result in battery damage.
- Maximum charge/discharge current: The maximum allowable current at which the battery can charge and discharge.

1.1.4. Cell Configurations

Li-ion batteries are manufactured in three forms: cylindrical, pouch, and prismatic as illustrated in Figure 1.3.

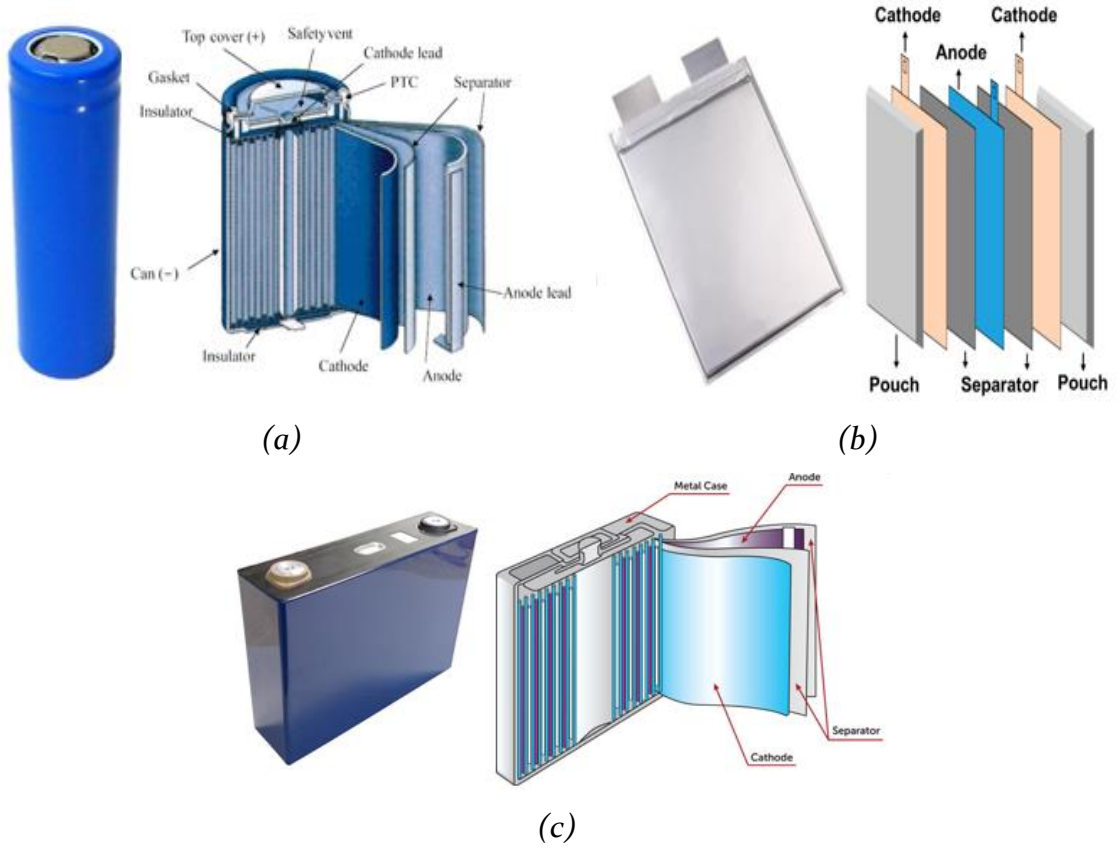

(a) *(b)*

(c)

Figure 1.3: Li-ion battery configurations

Cylindrical cells are more commonly used, however, prismatic and pouch cells are utilized for high-capacity battery applications to optimize the use of volume in high-capacity battery packs, since the electrodes have a larger surface area in a rectangular form [8]. Shown in Table 1.2 is a comparison of the advantages and disadvantages related to the different cell designs [10].

Table 1.2: Cell designs advantages and disadvantages

Form	Cylindrical	Pouch	Prismatic
Mechanical Strength	++	-	+
Thermal Management	-	+	+
Specific Energy	+	++	+
Energy Density	+	+	++

1.1.5. Electrode Chemistries

As discussed in 1.1.1, the cathodes are intercalation compounds from which Li^+ ions can diffuse from or in to. Currently, materials used to manufacture cathodes include Lithium Cobalt Oxide (LCO – $LiCoO_2$), Lithium Nickel Oxide (LNO – $LiNiO_2$), Lithium Manganese Oxide (LMO – $LiMnO_2$), Lithium Iron Phosphate (LFP – $LiFePO_4$), Lithium Nickel Manganese Cobalt (NMC – $Li(Ni_xMn_yCo_{1-x-y})O_2$) and Lithium Nickel Cobalt Aluminum Oxide (NCA – $Li(Ni_xCo_yAl_{1-x-y})O_2$). Moreover, there are two main types of anodes currently utilized in Li-ion battery, which include carbon-based electrodes such as graphite and graphene and Lithium Titanate (LTO – $Li_4Ti_5O_{12}$) [10]. A spider chart of the different Li-ion battery chemistries is illustrated in Figure 1.4 [11].

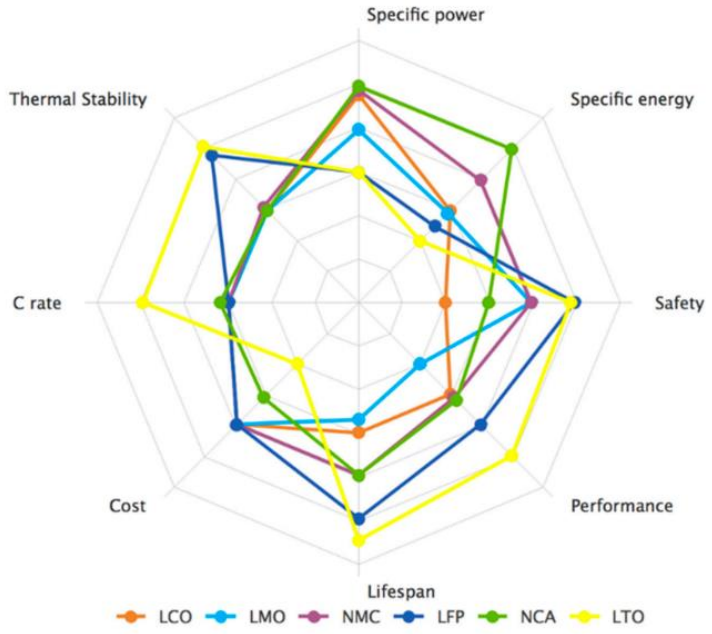

Figure 1.4: Spider chart for Li-ion batteries with different chemistries

Additionally, shown in Table 1.3 is a comparison of commercial Li-ion batteries and their characteristics [11]. The choice of battery selection is dependent upon the environment housing the cells in the pack, the required power output, the expected number of cycles (lifespan) and the application.

Table 1.3: Li-ion batteries characteristics

Cathode Chemistry	Nominal Voltage (V)	Specific Energy (Wh/kg)
LCO	3.7~3.9	150~200
LNO	3.6~3.7	150~200
LMO	3.7~4.0	100~150
NMC	3.8~4.0	150~220
LFP	3.2~3.3	90~130
NCA	3.6~3.65	200~260
LTO	2.3~2.5	70~85

1.1.6. Typical Cell Behavior

During charge and discharge, electrochemical reactions occur at the surfaces of electrodes. Moreover, the interface between the electrodes and electrolyte accumulates opposite charges to form a double layer, which behaves like a capacitor. Additionally, a resistance caused by the conductivity of the electrolyte and the distance between the electrodes is induced when electrons and charged particles traverse the electrolyte. Normally, the resistance and capacitance dominate the voltage response of a battery [12]. Furthermore, a typical voltage response of a battery subjected to a low, medium and high discharge rate, respectively, is shown in Figure 1.5 [13]. The cell starts at the upper voltage limit when fully charged and is discharged to its lower limit (cut-off voltage) when discharged.

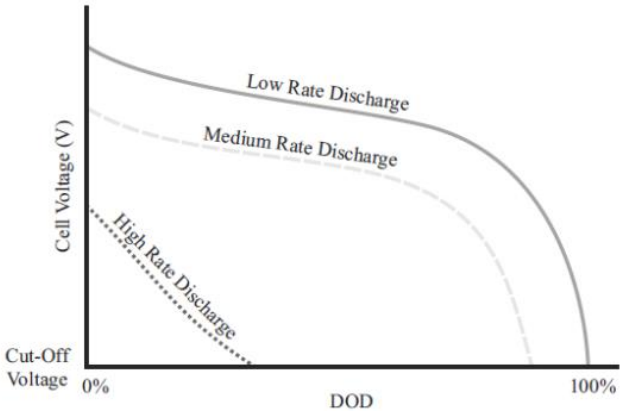

Figure 1.5: Voltage response of a Li-ion cell at different discharge rates

1.2. Contribution

The study conducted in this work proposes a novel coupled thermo-mechanical model to predict the dynamic and thermal behavior of various lithium-ion batteries. The dynamic system is an analogy based on a three-degree-of-freedom mass-spring system with damping. The system was decomposed into modal coordinates which represented the discharge of the battery, mass transport effect, and double-layer dynamic effect. Furthermore, the electrochemical heat generation rate was computed from the output states of the dynamic system and utilized as an input to the thermal models. The thermal models were used to predict the surface temperature of the battery during dynamic discharging conditions.

Additionally, the developed battery model is utilized to estimate the voltage response of a battery pack driving a benchtop brushless DC motor at varying speeds and under varying braking loads.

1.3. Thesis Structure

The thesis is structed as follows: Chapter 1 introduces the problem and the need for this research. Additionally, a brief overview of the history of Li-ion batteries and their market trajectory is presented. Then, a summary of how Li-ion batteries operate, basic terminology, the characteristics of their various forms and their voltage response are discussed. Chapter 2 gives an in-depth literature review of the dynamic models currently utilized to estimate the response of Li-ion batteries and

current advancements in research. Chapter 3 demonstrates the testing methodologies utilized in industry and research to characterize Li-ion batteries. Additionally, the experimental setup and data collected experimentally and from literature are presented in-depth. Chapter 4 displays the proposed novel mechanical analogy, derives the mathematical formulation of the dynamic analogy, a lumped thermal model, and a transient thermal model. Chapter 5 validates the proposed model by estimating the voltage and temperature responses of three Li-ion batteries and compares to the experimental data. Chapter 6 predicts the voltage response of battery pack the under dynamic loading of a brushless DC motor using the developed battery model. Finally, Chapter 7 concludes the efforts of the study conducted in this thesis with closing remarks and future work.

Chapter 2 Literature Review

Several electrochemical models have been developed to estimate the response of a battery at different charge and discharge rates and loading conditions. This chapter presents a brief review of the current state-of-the-art electrochemical models and the current advancements in literature.

2.1. Electrochemical Models

Lithium-ion battery modeling is complex due to its multi-domain, multi-physics nature. To compute the temperature distribution at the battery's length scale, the governing transport equations that occur in the anode-separator-cathode layers are solved [14].

The multi-scale, multi-domain electrochemical solution method computes the battery's thermal field through (2.1).

$$\frac{\partial \rho C_p T}{\partial t} - \nabla \cdot (k \nabla T) = \sigma_+ |\nabla \emptyset_+|^2 + \sigma_- |\nabla \emptyset_-|^2 + \dot{q}_{ECh} \qquad (2.1)$$

Where ρ, Cp, T, t and k are the density, heat capacity, temperature, time and thermal conductivity, respectively. Additionally, $\sigma+$ and $\sigma-$ are the positive and negative electrodes electrical conductivity, respectively. The phase potentials of the positive and negative electrodes are denoted by ø+ and ø-. Also, $\dot{q}_{ECh}$ is the electrochemical

reaction heat generation. Furthermore, the current flux is governed by (2.2) - (2.3), where *j* is the volumetric current density.

$$-j = \nabla \cdot (\sigma_{+} \nabla \varphi_{+}) \tag{2.2}$$

$$j = \nabla \cdot (\sigma_{-} \nabla \varphi_{-}) \tag{2.3}$$

Four electrochemical models have been widely reported in literature to estimate the impedance, voltage response and the heat generation of a battery, which are briefly discussed in the following subsections.

2.1.1. Impendence Spectroscopy

An electrochemical cell can be considered simply an impedance to a small sinusoidal excitation. The equivalent electrochemical circuit represents the performance of a battery cell through a network of resistors and capacitors that pass current with the same amplitude and phase angle that an actual battery cell does under a given excitation. This technique is known as Electrochemical Impedance Spectroscopy (EIS) [12]. Shown in Figure 2.1 is the Randle's equivalent circuit utilized to characterize the battery in the frequency domain.

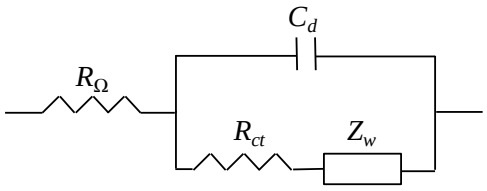

Figure 2.1: Randles equivalent circuit

The impedance of the cell at a given sinusoidal excitation and frequency range is described theoretically through (2.4) and (2.5) and graphically on a Nyquist plot as shown in Figure 2.2 [12].

$$Z_{Re} = R_{\Omega} + \frac{R_{ct} + \sigma\omega^{-\frac{1}{2}}}{(C_d\sigma\omega^{\frac{1}{2}} + 1)^2 + \omega^2 C_d^2 (R_{ct} + \sigma\omega^{-\frac{1}{2}})^2} \tag{2.2}$$

$$Z_{Im} = R_{\Omega} + \frac{\omega C_d (R_{ct} + \sigma\omega^{-\frac{1}{2}})^2 + \sigma\omega^{-\frac{1}{2}}(C_d\sigma\omega^{\frac{1}{2}} + 1)}{(C_d\sigma\omega^{\frac{1}{2}} + 1)^2 + \omega^2 C_d^2 (R_{ct} + \sigma\omega^{-\frac{1}{2}})^2} \tag{2.3}$$

Where ω is the angular frequency, R_{Ω} is the electrolyte resistance, R_{ct} is the charge transfer resistance that accounts for the voltage drop over the electrode-electrolyte interface, C_d is the double-layer capacitance that represents the effect of charges building up in the electrolyte at the electrode surface, and Z_W is the Warburg impedance. The Warburg impedance represents the diffusion of lithium ions in the electrodes and the resistance to mass transfer. Although valuable insights can be obtained from this technique, it cannot predict the battery run time or evaluate the dynamic behaviour at a fixed state-of-charge.

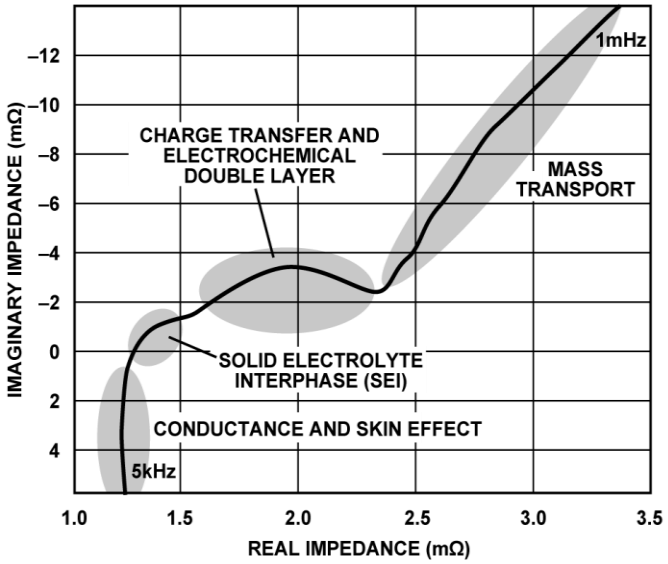

Figure 2.2: Nyquist plot of a typical Li-ion battery

2.1.2. NTGK Model

The Newman, Tiedemann, Gu, and Kim model (NGTK) is a semi-empirical electrochemical model proposed by Kwon *et al.* [15]. This method is regarded as the simplest electrochemical model as it requires the least inputs.

The volumetric current transfer rate is obtained utilizing the relationship displayed in (2.4),

$$j = \frac{Y[U - V]}{Vol} \tag{2.4}$$

where *Vol* denotes the volume of the battery. In addition, V is the terminal voltage which can measured experimentally or calculated from by φ_+ and φ_-. Furthermore, Y and U are the model parameters obtained experimentally as a function of the

battery's depth of discharge (DoD) and temperature. The DoD is expressed through (2.5). Where Q_{nom} is the nominal capacity of the battery.

$$DoD = \frac{Vol}{3600Q_{nom}} \int_0^t jdt \tag{2.5}$$

From the testing measurements, the relationship between Y and U and DoD and temperature is established through the 5th order polynomial equations (2.6) - (2.7),

$$U = \sum_{n=0}^{5} a_n(DoD)^n) - C_2\left(T - T_{ref}\right) \tag{2.6}$$

$$Y = \sum_{n=0}^{5} b_n(DoD)^n)\exp\left[-C_1\left(\frac{1}{T} - \frac{1}{T_{ref}}\right)\right] \tag{2.7}$$

where, a_n and b_n are the polynomial coefficients and C_1 and C_2 are the NTGK model constants for a specific battery to be determined experimentally. Also, T_{ref} is the reference temperature set at 298K. Additionally, the electrochemical heat generation is computed through (2.8).

$$\dot{q}_{ECh} = j\left[U - V - T\frac{dU}{dT}\right] \tag{2.8}$$

The first term in (2.8) describes the heat generated due to overpotential, whereas the second term is due to the entropic heating. A major limitation of this model is that only capable of predicting the voltage and temperature responses of Li-ion batteries under static loads.

2.1.3. The Equivalent Circuit Model

Chen and Rincon-Mora [16] proposed an 2nd order electrical circuit model to capture the dynamic characteristics of batteries, as shown in Figure 2.3.

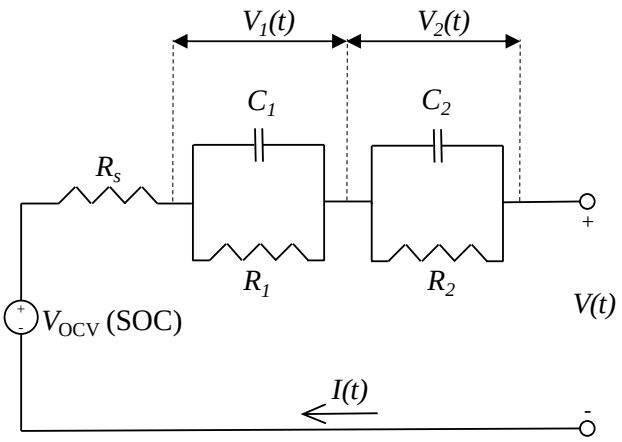

Figure 2.3: Equivalent Circuit Model

The electrical circuit consists of a voltage source that represents the open-circuit voltage (V_{OCV}), which describes the voltage across battery terminals when the cell is unloaded and in equilibrium. The resistor in series, R_s, is regarded as the ohmic resistance, which accounts for the power dissipated by the battery as heat. Additionally, the two resistor-capacitor sub circuits (R_1, R_2, C_1 & C_2) represent the time constants in the circuit, which account for the diffusion dynamics of the battery [8]. The input to this circuit is the current drawn from the battery, *I(t)*. The output of the system is the measured voltage drop across the passive components of the circuit subtracted from V_{OCV} to obtain the voltage delivered by the battery. An

important parameter to evaluate and estimate in an electrochemical cell is the SOC, computed through (2.9).

$$SOC\ (t) = SOC_0 - \int_{t_0}^{t} \frac{I\ (t)}{Q_{nom}} dt \tag{2.8}$$

Where SOC_o is the initial state of charge of the battery tested and $I\ (t)$ is the measured current. Furthermore, the voltage-current relationship is established through (2.9) - (2.11).

$$V = V_{OCV}(SOC) - V_1 - V_2 - R_S(SOC)I(t) \tag{2.9}$$

$$\frac{dV_1}{dt} = -\frac{1}{R_1(SOC)C_1(SOC)}V_1 - \frac{1}{C_1(SOC)}I(t) \tag{2.10}$$

$$\frac{dV_2}{dt} = -\frac{1}{R_2(SOC)C_2(SOC)}V_2 - \frac{1}{C_2(SOC)}I(t) \tag{2.11}$$

The parameters in (2.10) – (2.11) are identified by numerically tuned as a function of SOC to fit the experimental data of a dynamic testing. Additionally, the heat generation rate of the battery is computed through (2.12).

$$\dot{q}_{ECh} = \frac{I(t)}{Vol}\left[V_{OCV} - V - T\frac{dU}{dT}\right] \tag{2.12}$$

Moreover, reduced order models of the equivalent circuit have been investigated in literature to reduce the parameters required to be estimated the circuit to characterize the response of the battery [16]. Shown Figure 2.4 are the 0th order and 1st order equivalent circuit (ECM) models.

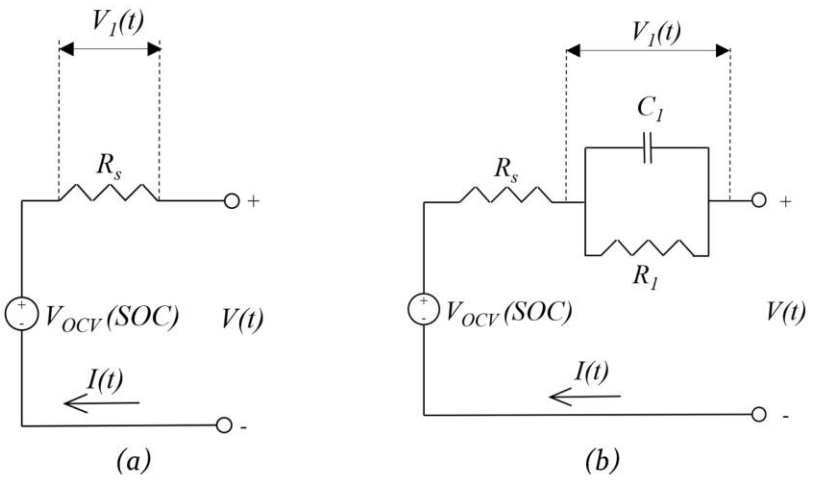

Figure 2.4: (a) 0^{th} order ECM (b) 1^{st} order ECM

Depending on the dynamics required to be captured from the voltage response of the battery, the order of the ECM is chosen. Rapid dynamics are generally captured by a higher order model. The battery equivalent circuits are the most used models to represent and estimate Li-ion battery dynamics due to their low computation time and high accuracy; however, higher order models yield to more tunable parameters which increases the complexity of the model.

2.1.4. Newman's P2D Model

The P2D model is a physics based electrochemical model that can accurately capture the Li-ion migration utilizing the porous electrode and concentration solution theories [14]. Figure 2.5 illustrates the electrode and particle domain in the P2D model [17].

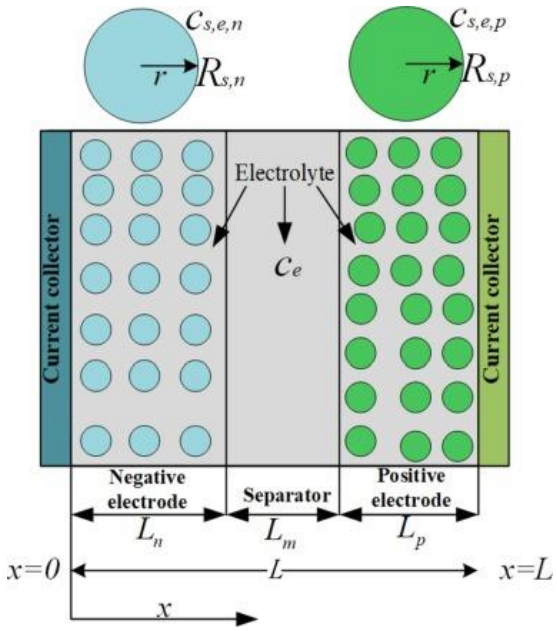

Figure 2.5: Electrode and particle domain

Lithium diffuses from the surface of the negative to the positive electrode during discharge, which endures an electrochemical reaction. This reaction releases electrons and transfers the lithium into the electrolyte phase. A similar reaction takes place which transfers the lithium from the electrolyte phase to the solid positive electrode phase.

The charge and mass conservation laws govern the lithium-ion transport phenomena. The lithium conservation equations solved in the *r*-dimension of the spherical particles in solid and electrolyte phases are described in (2.13) – (2.14).

$$\frac{\partial c_s}{\partial t} = \frac{D_s}{r^2}\frac{\partial}{\partial r}\left(r^2 \frac{\partial c_s}{\partial r}\right) \tag{2.13}$$

$$\frac{\partial(\varepsilon_e c_e)}{\partial t} = \frac{\partial}{\partial x}\left(D_e \varepsilon_e^{\beta} \frac{\partial c_e}{\partial x}\right) + \frac{1 - t_+^0}{F} j^{Li} \tag{2.14}$$

Where c_s and c_e are the phase and concentrations in the solid and electrolyte phase, respectively. D_s and D_e are the diffusion coefficients of the Li and the Li+ in solid and electrolyte phase. Additionally, t_+^0 is the transference number of the lithium ion, F is Faraday constant and ε_e is the volume fraction of the electrolyte phase in electrode. Also, β is the Bruggeman porosity exponent. Additionally, the charge conservation in solid and electrolyte phases are computed through (2.15) - (2.16),

$$\frac{\partial}{\partial x}\left(\sigma \varepsilon_s^{\beta} \frac{\partial \varphi_s}{\partial x}\right) - j^{Li} = 0 \tag{2.15}$$

$$\frac{\partial}{\partial x}\left(\sigma \varepsilon_s^{\beta} \frac{\partial \varphi_s}{\partial x}\right) + \frac{\partial}{\partial x}\left(k_D^{eff} \frac{\partial ln c_e}{\partial x}\right) + j^{Li} = 0 \tag{2.16}$$

here ε_s is the volume fraction of the active material in the electrode. Additionally, k_D^{eff} is the electrolyte diffusional conductivity and is defined through (2.17).

$$k_D^{eff} = \frac{2RTk\varepsilon_e^{\beta}}{F}(t_+^0 - 1)\left(1 + \frac{dlnf_{\pm}}{dlnc_e}\right) \tag{2.17}$$

Moreover, the volumetric current transfer rate is expressed as a function of the overpotential, η, through the Bulter-Volumer equation displayed in (2.18).

$$j^{Li} = \frac{3\varepsilon_s}{r_s} i_0 \left\{\exp\left(\frac{\alpha_a F}{RT}\eta\right) - \exp\left(\frac{-\alpha_c F}{RT}\eta\right)\right\} \tag{2.18}$$

Where α_a and α_c are the charge transfer coefficients at the anode and cathode, respectively. The exchange current density, i_o is defined through (2.19).

$$i_0 = k_m(c_e)^{\alpha_a}(C_{s,max} - c_{s,e})^{\alpha_a}(c_{s,e})^{\alpha_c} \tag{2.19}$$

From equation (2.19), k_m is the reaction rate constant and $C_{s,max}$ is the maximum concentration of lithium in solid phase.

Furthermore, the volumetric current transfer rate due to the electrochemical reactions is expressed through (2.20),

$$j_{ECh} = -\frac{i_p}{Vol} \tag{2.20}$$

where i_p is the transverse current density and computed through (2.21).

$$i_p = \int_0^{l_p} j^{Li} dx \tag{2.21}$$

Finally, (2.22) is utilized to compute the heat generation rate in the battery during the charge/discharge process.

$$\dot{q}_{ECh} = \frac{i_p V + \int_{l_p+l_s+l_n}^{0} j^{Li}\left(T_{ref}\frac{\partial U}{\partial T} - U_{Ref}\right)dx}{l_p + l_s + l_n} \tag{2.22}$$

Where l_p, l_n and l_s are the thicknesses of the positive electrode, negative electrode, and the separator. A major disadvantage of the P2D model is its computational complexity. Additionally, it requires the user to have extensive knowledge and understanding regarding the chemical parameters of the battery. Additionally, the identification of many parameters in model makes it not very practical and difficult to apply in engineering applications.

2.1.5. Current Literature

Several studies have focused on enhancing the parameter estimation method used in equivalent circuit models [17]–[20]. Hau et al. [21] optimized passive circuit components as a function of the SOC and different temperature levels. In addition, they were able to evaluate these parameters for different input current profiles to capture the different time constants that a lithium-ion battery cell exhibits during underload operation and compare them with the relaxation period. Zhang et al. [22] proposed a new decoupled weighted recursive least-squares method to separately estimate the battery's slow and fast dynamics. Through this method, they were also able to estimate the SOC of the cell tested. Hariharan et al. [23] developed a nonlinear equivalent circuit model for lithium-ion cells, in which the circuit elements were evaluated based on the charge transfer reaction and variable resistance. Their state-space model was used to resolve the overall cell potential into potential drops due to ionic conductivity, charge transfer reactions, and solid-phase diffusion. Liu et al. [24] proposed a controlled auto-regression and moving-average-based equivalent circuit to fully consider the effects of measurement errors and the dynamic external electrical properties of lithium-ion batteries and estimate the state-of-charge using a Kalman filter. Similarly, Wei et al. [25] developed a method to integrate recursive total least squares with a state of charge observer to enhance the estimation of the model parameters and the state of charge. Their technique was able to reduce the noise effects from the experimental measurement to estimate the

parameters and the state of charge more accurately and robustly. Li et al. [26] designed an ensemble-based state estimator using a singular evolutive interpolated Kalman filter to obtain the internal states of a lithium-ion battery cell. In addition to that, they characterized the heat transfer along the electrode width direction through the finite volume method. Through their model, they were able to predict the internal behavior of the battery regardless of the operating conditions. Wu et al. [27] proposed a knowledge-based, battery temperature and health constrained battery management strategy for a hybrid electric bus. They were able to double the training efficiency with the integration of the expert-assistance system. Additionally, the developed model maintained the internal battery temperature below a particular safety threshold and reduced the driving cost by 23.9% compared to other state-of-the-art models.

Furthermore, Paschero et al. [28] proposed a mechanical analogy to characterize a battery cell to enhance the state of charge estimation. They related the stored charge in an electrochemical cell relative to current and voltage measurements to estimate the volume of water stored in a reservoir with nonlinear walls based on pressure and flow rate measurements. Utilizing the equivalent circuit model and its hydraulic mechanical analogy, the battery states were estimated using a Kalman filter. Wei et al. [29] proposed a technique that assimilates the Frisch scheme-based bias compensating recursive least squares (FBCRLS) with a SOC observer to improve the parameters and the state of charge estimation. Furthermore, the model utilizes an

online estimation of the noise statistics and recompenses the noise effect so that the model parameters can be extracted without bias.

Moreover, Zheng et al. [30] established two SOC estimators based on two OCV tests, a low-current OCV test, and an incremental OCV test. The open-circuit voltage and state of charge relationship were determined to be dependent upon the operating temperature. This was accomplished by comparing the accuracy of both SOC estimators suggested. It was found that the estimator based on the incremental OCV test showed higher accuracy at 25°C and 45°C; however, the estimator based on the low-current OCV test provided a higher resolution at 0°C.

Hu *et al.* [31] developed an aging-robust and disturbance-immune ISC diagnostic method for lithium-ion batteries. The authors incorporated a multi-state-fusion ISC resistance estimator and a RTLS-VF-based bias compensator within a universal model switching. Their proposed model was able to accurately estimate the ISC resistance and outperform the state-of-the-art techniques in the noise immunity. She *et al.* [32] established a technique of applying the incremental capacity analysis (ICA) method for battery pack-level state-of-health (SOH) estimation in real-world situations. It was found that the study they conducted provided a scheme of applying the ICA-based method to accurately predict the SOH in a pack-level battery. Wang *et al.* [33] proposed a data-driven method for charging capacity diagnosis based on real-world EV operating data. The input to their three-based prediction model were the charging rate, temperature, state-of-charge and

accumulated driving mileage. The battery charging capacity abnormity is diagnosed through a statistics-based method by analyzing the error distribution of large sets of data. Hu *et al.* [34] presented an SOC and SOH co-estimation scheme based on the fractional-order calculus. They used the fractional-order equivalent circuit model to predict the voltage response utilizing a Hybrid Genetic Algorithm/Particle Swarm Optimization method. Then, a fractional order extended Kalman filter was used to estimate the SOC and SOH. It was found that this technique demonstrated high accuracy with a steady-state error of 1% for both SOC and SOH.

Thermal management of battery systems is also a critical factor to consider in the design of a battery pack as it impacts the performance of the cells and can lead to catastrophic fire incidents if not managed appropriately. The heat generated from a battery is due the complicated electrochemical reactions taking place in the cell [35]. These reactions vary with time, temperature and current distribution; therefore, there is a need for a simple and intuitive dynamic model to predict the heat generated by a battery to obtain essential thermal parameters under dynamic discharging conditions.

Various studies have been conducted to develop accurate thermal models to estimate the heat generation rate and the temperature profile of batteries [36], [37]. Chiew *et al.* [38] developed a pseudo three-dimensional coupled electro-thermal model to investigate the thermal behavior of a cylindrical LFP battery under various discharge rates and temperatures. They used a series of regression models to

quantify the thermal behavior of the battery and demonstrated how the performance of the battery differs at lower ambient temperatures and discharge rates. Mahamud and Park [39] proposed a thermal management method utilizing a reciprocating air flow for cylindrical Li-ion cells. They numerically analyzed their model utilizing a two-dimensional computational fluid dynamics (CFD) model and a lumped thermal-capacitance model. Their numerical results indicated that the reciprocating flow yielded to a 72% temperature drop in the battery system.

Furthermore, Zhang [40] investigated the heat generation characteristics of a cylindrical lithium-ion battery by using a coupled electro-thermal model. He analyzed the thermal characteristics of the battery by employing the finite volume numerical method that considered the electrolyte transport properties as a function of temperature and Li-ion concentration. It was found that the Ohmic heat contributed to 54% of the total heat generation in the battery, whereas the heat generated from the electrochemical reactions yielded to almost 30%.

In addition, Panchal *et al.* [41] presented a mathematical model to predict the transient temperature distribution of a prismatic battery under four constant current discharge rates. Their mathematical model was able to predict the surface temperature within proximity compared to the experimental measurements. Ye *et al.* [42] developed an electro-thermal cycle life model by accounting for the thermal and capacity fading effects. With their model, they were able to predict the capacity lost and the temperature at different cycle number and the effects the temperature

had on the capacity. Haung *et al.* [43] established a co-simulation thermoelectric model for a Lithium-ion battery. They combined the equivalent circuit model with CFD to characterize the thermal and electrical behavior of the battery. Their results indicate that their method with the temperature correction has higher accuracy than the traditional thermal simulation without the temperature correction. Wang *et al.* [44] proposed a finite element thermal model for cylindrical Lithium-ion battery to address the inconsistency issues of temperature distribution among battery cells in a battery pack. Through their model, they were able to characterize the discharge thermal behavior and predict the temperature profile within a small proximity at varied ambient temperatures.

Furthermore, Li *et al.* [45] established a computationally efficient state estimation method for lithium-ion batteries. Their technique is based on a degradation-conscious, high-fidelity, electrochemical-thermal model for battery management systems. They were able to significantly improve the state estimation by employing an ensemble-based state estimator using the singular evolutive interpolated Kalman filter.

Chapter 3 Experimental Approaches & Data Acquisition

This chapter discusses the following: first, a brief introduction about the experimental methodologies utilized to characterize the static and dynamic responses of Li-ion batteries are illustrated, then the experimental setup developed to measure the data and the data collected are detailed and lastly, the data utilized from open-access sources is presented.

3.1. Experimental Methodologies

3.1.1. Static Capacity Test

This objective of this test is to experimentally determine the capacity of the cell. The capacity of a cell is usually given by the manufacturer; however, due to mechanisms such as aging or capacity fading, the capacity of a battery can degrades over time.

The test is conducted by discharging a Li-ion battery at a constant C-rate [46]. The discharge begins at a fully-charged-state at the upper voltage limit (V_{max}) and ends at the cut-off voltage (V_{min}). Shown in Figure 3.1 are the constant current profile and the voltage response of the cell. The capacity can then be determined through (3.1).

$$Q = \frac{I\Delta t}{\Delta SOC} \tag{3.1}$$

Where I is the current, t is time and SOC is the state-of-charge of the battery.

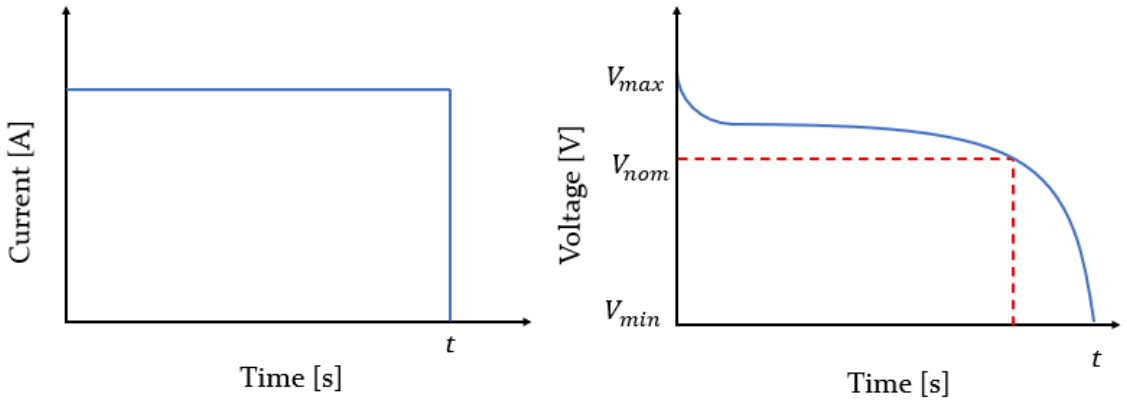

Figure 3.1: Static discharge test

3.1.2. Hybrid Pulse Power Characterization Test

The Hybrid Pulse Power Characterization (HPPC) test is a testing methodology to determine the power dynamic characteristics of a battery over the cell's usable voltage range. The load profile incorporates both charge/discharge and regeneration pulses that occur at various states of charge (SOC), as shown in Figure 3.2. After every current discharge pulse, the SOC of the battery drops relative to the C-rate and the pulse period. Similarly, after a charging pulse, the SOC increases relative to C-rate and the pulse period. Additionally, after every charge/discharge pulse, the battery is rested for a period called regeneration to obtain the open-circuit voltage of the cell with respective to the SOC; therefore, a full nonlinear OCV as a function of SOC can be known. A detailed insight is given in Figure 3.3 which illustrates a single discharge current pulse and the voltage response [47].

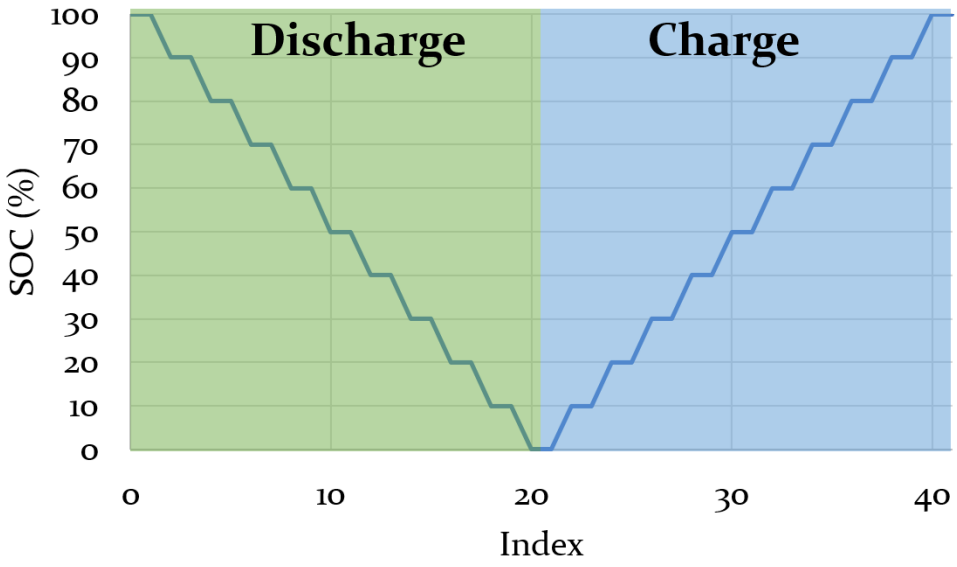

Figure 3.2: HPPC testing SOC profile

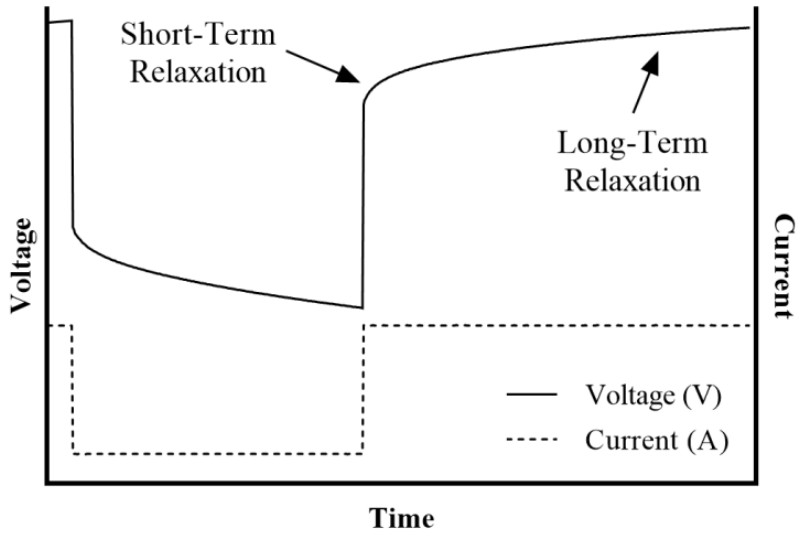

Figure 3.3: HPPC voltage response

3.2. Experimental Procedures & Approaches

To measure the current and voltage responses conveniently and effectively across the batteries, the experimental setup shown in Figure 3.4 was employed. The circuit was constructed from a DC electronic load (BK Precision 8601) to discharge the battery at consistent current level, a relay to actuate when the current is drawn from the battery, a microcontroller (Arduino MEGA2560 R3) to trigger the relay at a consistent duty cycle and generate the current square waves. Additionally, two multi-meters (Keysight 34465A 6 ½) were utilized to measure the current and the voltage of the battery. For the cylindrical cells, the first multi-meter was connected in series to record current, whereas the second one was connected in parallel to measure the voltage response across the battery. Whereas, for the pouch cell, a shunt resistor was utilized to measure the current; therefore, the second multi-meter was connected in parallel with the shunt to measure the voltage drop across, which was then converted to current. Furthermore, a K-type thermocouple connected to a data acquisition system (DAQ) (OMEGA OM-CP-QuadTemp2000digital) was used to record the temperature values. The sampling rate on the multimeters are 0.4 Sa/s whereas the thermocouple DAQ is set to a sampling rate of 2 Sa/s. In addition, the microcontroller triggered the relay at constant frequency of 2.8mHz.

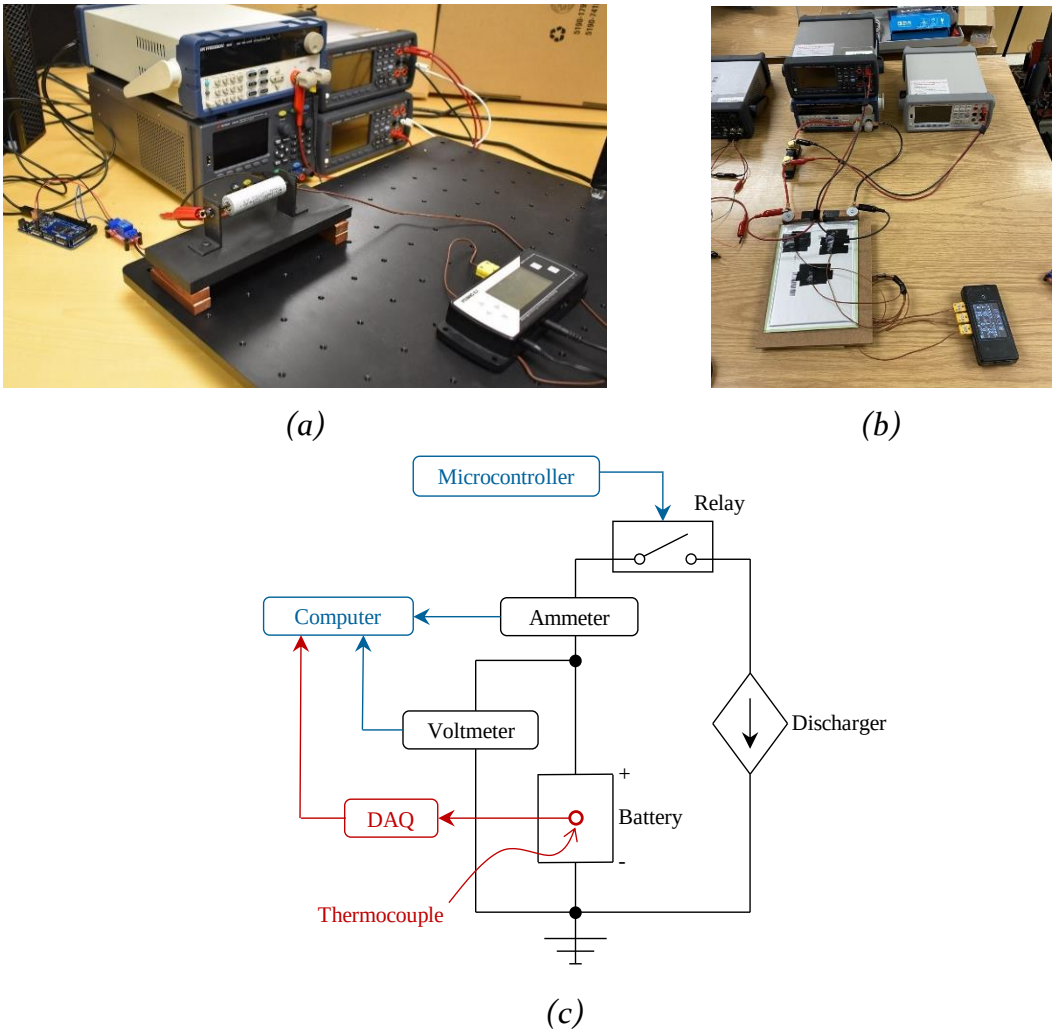

Figure 3.4: (a) Experimental test rig for cylindrical cells (b) Experimental test rig for pouch cell (c) Circuit schematic

Two cylindrical Lithium-ion batteries are tested. The first battery is a Panasonic NCR27100 [48] and the second cell is a Samsung INR18650-25R [49]. Listed in Table 3.1 are the specifications for the batteries utilized.

Table 3.1: Cylindrical batteries specifications

Parameter	Panasonic NCR27100	Samsung INR18650-25R
Nominal capacity (mAh)	4800	2500
Nominal voltage (V)	3.6	3.6
Maximum Voltage (V)	4.2	4.2
Cut-Off voltage (V)	2.5	2.5
Dimensions (mm)	21Ø × 70	18.33Ø × 64.85
Mass (g)	68.5	45

Furthermore, the pouch cell tested is a LG Chem battery. The specifications presented in Table 3.2 were derived from [50] and physical measurements done.

Table 3.2: LG Chem cell specifications

Parameter	LG Chem
Nominal capacity (Ah)	15
Nominal voltage (V)	3.7
Maximum Voltage (V)	4.15
Cut-Off voltage (V)	3.0
Dimensions (mm)	160 × 200 × 5
Mass (g)	68.5

To determine the dynamic performance of the batteries, the cells were tested in accordance with the HPPC methodology. The load profile incorporates a discharge and regeneration pulses at different SOC levels, revealing the dynamic voltage response of the battery. Additionally, two discharge rates were considered, 1C and 2C. Shown in Figure 3.5 are the testing data for the Samsung INR18650-25R battery.

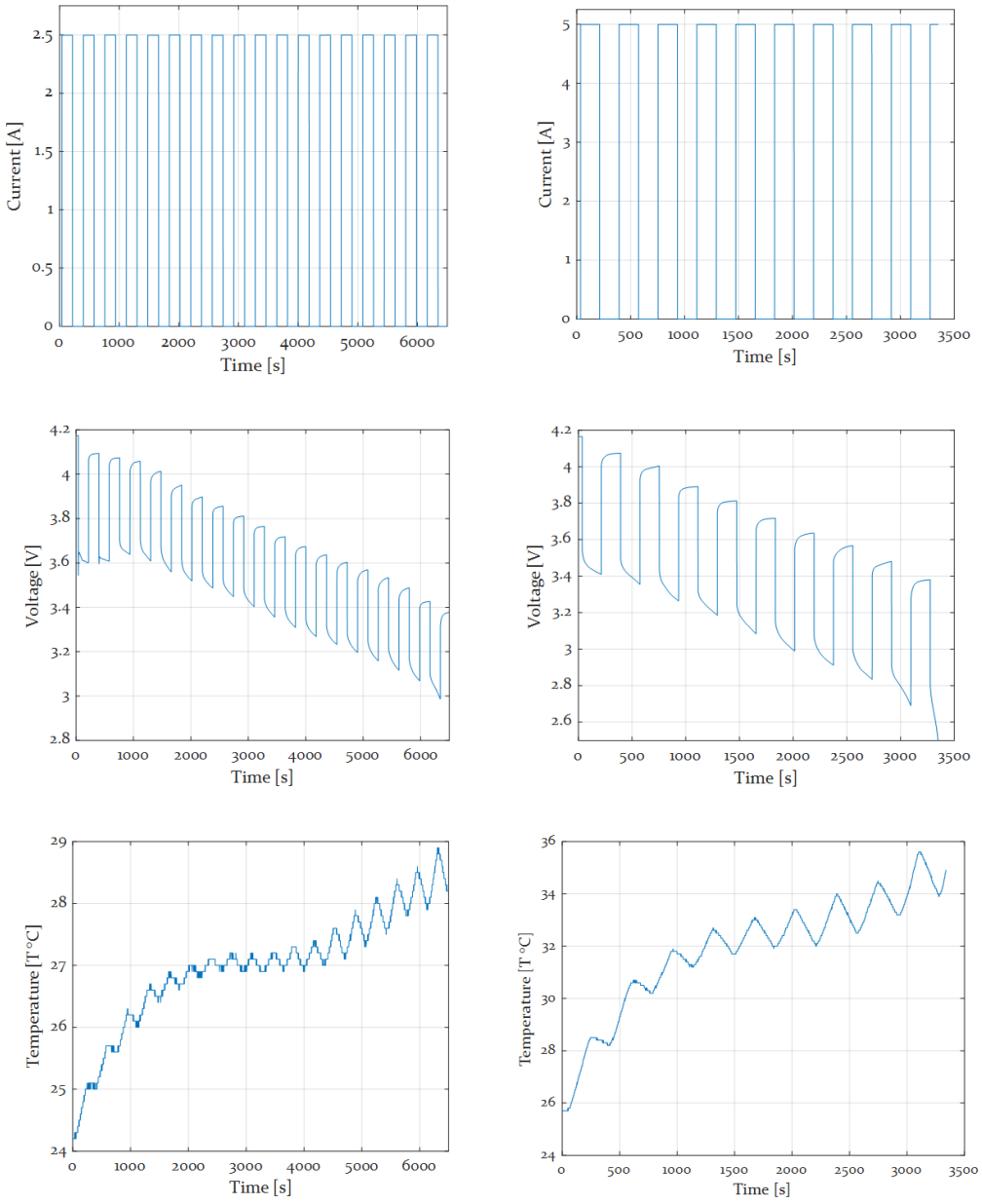

Figure 3.5: Samsung INR18650-25R testing data (a) 1C (b) 2C

Figure 3.5 (a) displays the measured data at 1C. The discharge current was set to pulse the battery at 2.5A; therefore, discharging the battery in two hours, since the

battery was allowed to rest. Additionally, Figure 3.5 (b) displays the testing data at 2C, where the discharge current was set to pulse the battery at 5A, discharging the battery in an hour.

Furthermore, the testing data for the Panasonic NCR27100 battery is displayed in Figure 3.6. The battery was pulsed at two discharge rates, 1C and 2C. Like the Samsung INR18650-25R, the discharge current, voltages and temperatures were recorded for both discharge rates.

Additionally, the testing data for the LG Chem battery is illustrated in Figure 3.7. An HPPC test at a discharge rate of C/3 was carried out to reveal the dynamics of the battery and a static discharge test at 17.5A was conducted to estimate the temperature contours of the cell.

Moreover, for both cells, the voltage response was utilized to characterize the dynamic effects such the mass transfer and double layer on the discharge of the battery, whereas the temperature response was used to estimate the thermal parameters of the cells under dynamic loading.

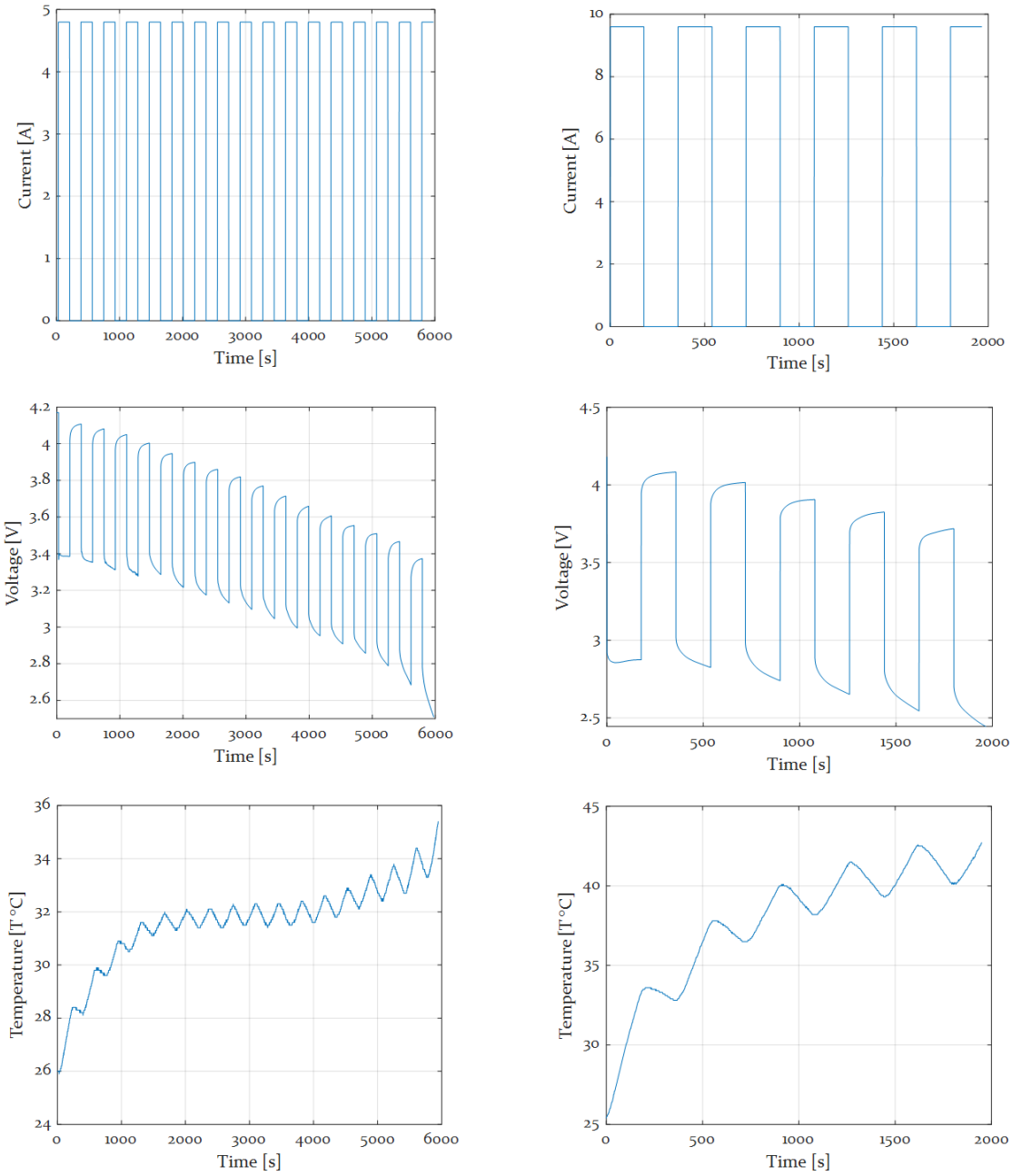

Figure 3.6: Panasonic NCR27100 testing data (a) 1C (b) 2C

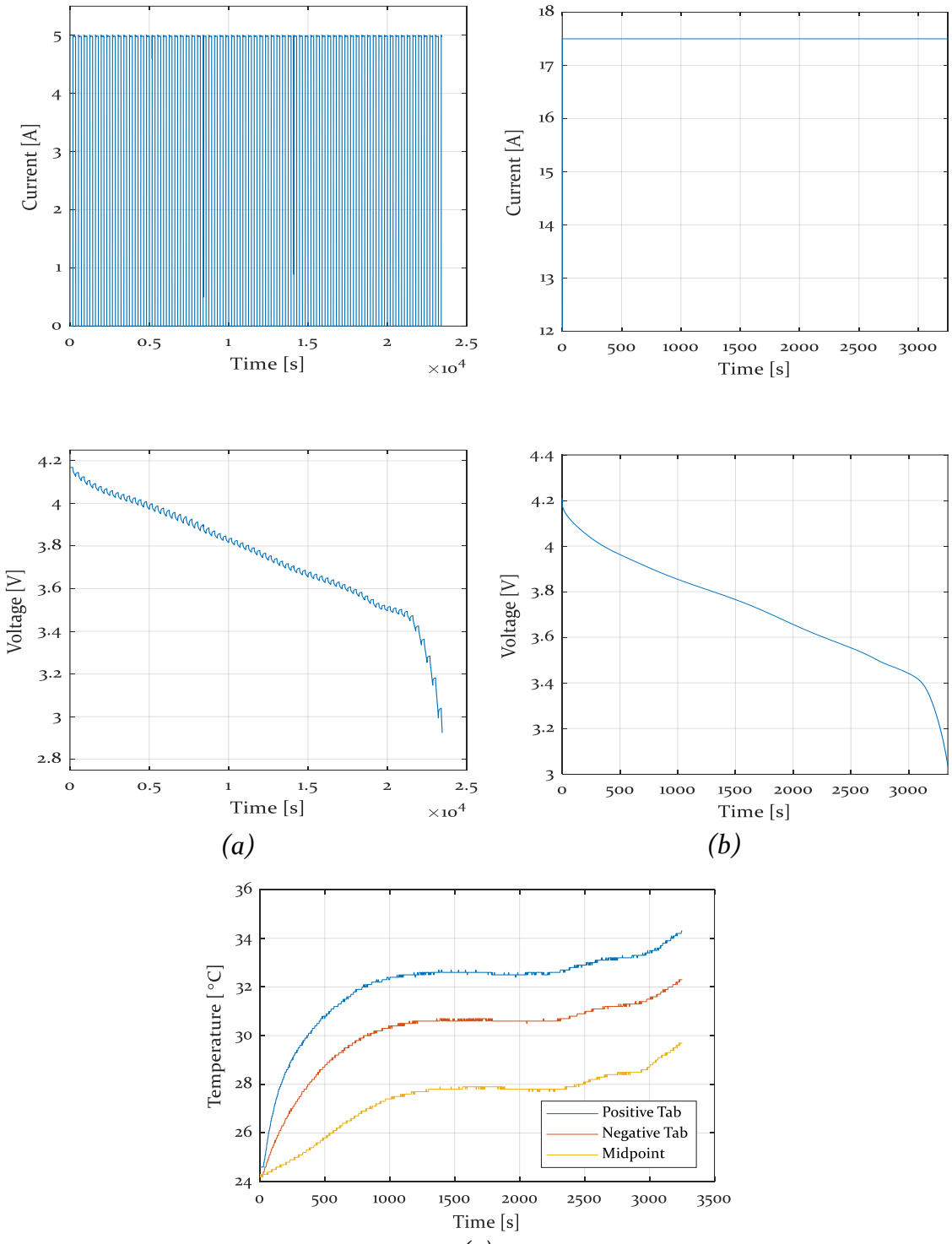

Figure 3.7: LG Chem testing data (a) 5A HPPC (b) 17.5A static discharge (c) 17.5A static discharge temperatures

3.3. Open-Access Data

Two datasets developed by the Center for Advanced Life Cycle Engineering (CALCE) [51] for a Samsung INR18650-20R battery were utilized. Shown in Table 3.3 are the parameters of the battery tested [52].

Table 3.3: Samsung INR18650-20R battery specifications

Parameter	INR 18650-20R
Chemical system	LiNiMnCo /Graphite
Form factor	Cylindrical
Nominal capacity (mAh)	2000
Maximum voltage (V)	4.2
Nominal voltage (V)	3.6
Cut-Off voltage (V)	2.5
Dimensions (mm)	18.33Ø × 64.85
Mass (g)	45

The first dataset was an incremental current OCV test, where the battery was pulsed at a constant current at 25°C. The current load profile allowed the battery to rest until the relaxation period reached steady state; therefore, the OCV-SOC relationship was established. The second dataset was a low current OCV test at which the battery was discharged at a constant C/20 rate at 25°C to estimate that the terminal voltage corresponded to OCV. Shown in Figure 3.8 are the testing data for both tests.

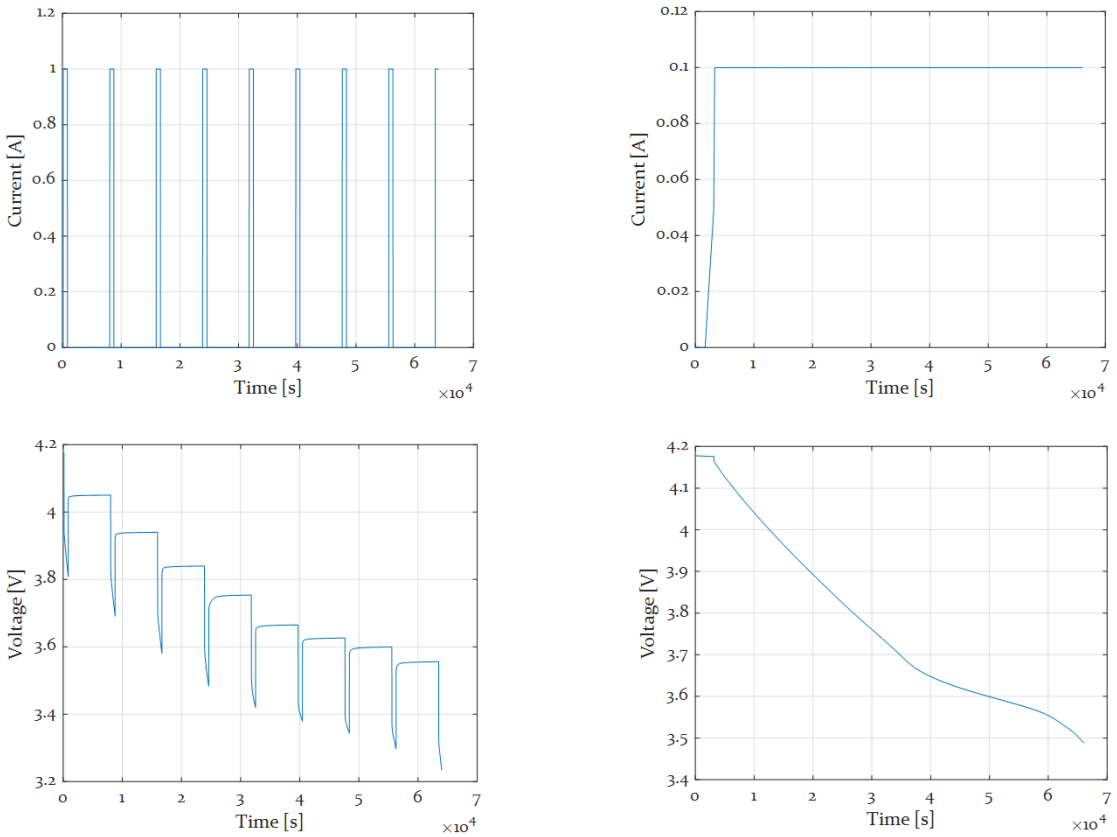

Figure 3.8: Samsung INR18650-20R data (a) incremental current OCV (b) low current OCV

For the incremental current OCV test, the battery was pulsed with 1A for 12 minutes and allowed to recover for 2 hours to reach steady state, whereas for the low current OCV test, the battery was discharged at 0.1 A for almost 17 hours. The primary goal of the low current OCV test was to validate that the OCV of the battery corresponded to the measure terminal voltage.

Chapter 4 A Novel Coupled Thermo-Mechanical Battery Dynamic System

The method developed in this thesis and detailed in this chapter is a novel mechanical analog for battery dynamics which is useful because of its ability to achieve accurate predictions for the voltage response and heat generation of Li-ion batteries [53], [54]. Additionally, it is intuitive to work with despite being higher order. Furthermore, since the system is modally decomposed, each degree of freedom can be analyzed independently adhering to the different dynamic effects. The estimated heat generated by the battery is then used as an input to thermal models to predict surface temperature of cylindrical and pouch cells, as shown in Figure 4.1.

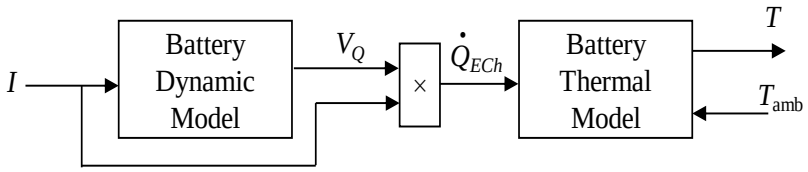

Figure 4.1: Thermo-mechanical coupled system.

Here, V_Q is the the overpotential voltage predicted by the dynamic model. The following subsections outline the theory and derives the governing equations of the coupled models.

4.1. Mathematical Derivation

4.1.1. Mechanical Analogy

When a battery is discharged, the current is drawn out and the voltage that the battery can supply degrades over time. However, when the current load is removed, a portion of the voltage can recover, depending on the internal characteristics and properties of the cell. A mechanical system that behaves similarly is shown in Figure 4.2.

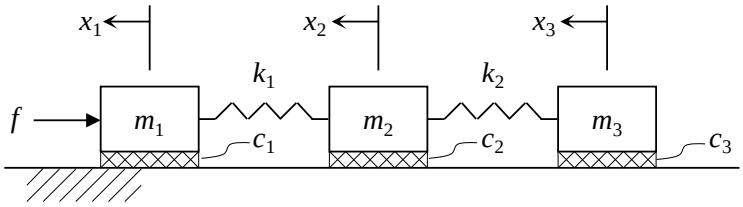

Figure 4.2: Three-degree-of-freedom damped spring-mass system analogy of a battery dynamics.

As the external force *f* pushes mass m_1, the entire spring-mass-damper system tends to slide to the right. The overall motion represents the battery discharge. If the external force is removed, the compressed springs $k_1$and k_2 can decompress and recover a portion of the m_1 and m_2 displacements, although the overall displacement has moved negatively and does not recover. Note that each mass is connected to another mass by a spring; however, there is no spring-to-ground connection. This phenomenon mirrors the dynamic discharge characteristics of the electrochemical

cells. Furthermore, each mass was damped by a viscous damping component c_1, $c_2$and c_3 to the ground. This term limits the discharge rate and stops discharging when there is no load applied. To model this system, free-body diagrams were developed, in which all physical contacts were severed and replaced by forces, as shown in Figure 4.3.

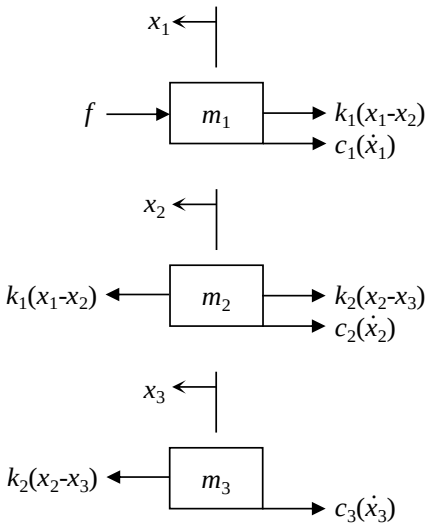

Figure 4.3: Free-body diagrams of the mechanical analogy

The equations of motion for each nodal point were based on Newton's second law of motion. The equations of motion were assembled in a coupled system (5.1),

$$\begin{cases} m_1\ddot{x}_1 + c_1(\dot{x}_1) + k_1(x_1 - x_2) = -f \\ m_2\ddot{x}_2 + c_2(\dot{x}_2) + k_2(x_2 - x_3) - k_1(x_1 - x_2) = 0 \\ m_3\ddot{x}_3 + c_3(\dot{x}_3) - k_2(x_2 - x_3) = 0 \end{cases} \tag{5.1}$$

where m_1, m_2, and m_3 are the masses, respectively. In addition, c_1, c_2, and c_3 *are* the damping coefficients, and k_1, k_2, and k_3 are the spring stiffnesses. Furthermore, f

denotes the load externally applied to the system. Finally, x, $\dot{x}$, and $\ddot{x}$ are the position, velocity, and acceleration, associated with each mass, respectively. The system of equations (5.1) is expressed in matrix form (5.2):

$$\begin{bmatrix} m_1 & 0 & 0 \\ 0 & m_2 & 0 \\ 0 & 0 & m_3 \end{bmatrix} \begin{Bmatrix} \ddot{x}_1 \\ \ddot{x}_2 \\ \ddot{x}_3 \end{Bmatrix} + \begin{bmatrix} c_1 & 0 & 0 \\ 0 & c_2 & 0 \\ 0 & 0 & c_3 \end{bmatrix} \begin{Bmatrix} \dot{x}_1 \\ \dot{x}_2 \\ \dot{x}_3 \end{Bmatrix} + \begin{bmatrix} k_1 & -k_1 & 0 \\ -k_1 & k_1 + k_2 & -k_2 \\ 0 & -k_2 & k_2 \end{bmatrix} \begin{Bmatrix} x_1 \\ x_2 \\ x_3 \end{Bmatrix} = \begin{bmatrix} -1 \\ 0 \\ 0 \end{bmatrix} \{f\} \tag{5.2}$$

The forced response of a multiple-degree-of-freedom system can be computed using modal analysis [55]. To make the transformation convenient, the system is written as the matrix (5.3).

$$M\ddot{\boldsymbol{x}} + \boldsymbol{C}\dot{\boldsymbol{x}} + \boldsymbol{K}\boldsymbol{x} = \boldsymbol{B}\{f\} \tag{5.3}$$

M, **C**, **K**, and **B** are the mass, damping coefficient, spring stiffness, and input matrices, as expressed in (5.4), (5.5), (5.6), and (5.7).

$$\boldsymbol{M} = \begin{bmatrix} m_1 & 0 & 0 \\ 0 & m_2 & 0 \\ 0 & 0 & m_3 \end{bmatrix} \tag{5.4}$$

$$\boldsymbol{C} = \begin{bmatrix} c_1 & 0 & 0 \\ 0 & c_2 & 0 \\ 0 & 0 & c_3 \end{bmatrix} \tag{5.5}$$

$$\mathbf{K} = \begin{bmatrix} k_1 & -k_1 & 0 \\ -k_1 & k_1 + k_2 & -k_2 \\ 0 & -k_2 & k_2 \end{bmatrix} \tag{5.6}$$

$$\mathbf{B} = \begin{bmatrix} -1 \\ 0 \\ 0 \end{bmatrix} \tag{5.7}$$

The position of each mass, velocity and acceleration can be defined in terms of an intermediate coordinate system **q**, as shown in (5.8), (5.9), and (5.10).

$$\boldsymbol{x} = \boldsymbol{M}^{(-1/2)}\boldsymbol{q} \tag{5.4}$$

$$\dot{\boldsymbol{x}} = \boldsymbol{M}^{(-1/2)}\dot{\boldsymbol{q}} \tag{5.5}$$

$$\ddot{\mathbf{x}} = \mathbf{M}^{(-1/2)}\ddot{\mathbf{q}} \tag{5.6}$$

The damping matrix is a linear combination of the mass and stiffness matrices, known as proportional damping (5.7).

$$\boldsymbol{C} = \alpha\boldsymbol{M} + \beta\boldsymbol{K} \tag{5.7}$$

where α and β are the scalar constants. The damping of the proportional form allows for decoupling of the modal equations of motion. Inspecting the forms of (5.4) - (5.6) no mass has stiffness to ground; therefore, to achieve proportional damping, the constant β is assumed to be zero. Equation (5.7) can be simplified to (5.8).

$$\boldsymbol{C} = \alpha\boldsymbol{M} \tag{5.8}$$

Furthermore, the equation of motion can be written in terms of the coordinate system **q**, as shown in (5.9),

$$\boldsymbol{I}\ddot{\boldsymbol{q}} + \widetilde{\boldsymbol{C}}\dot{\boldsymbol{q}} + \widetilde{\boldsymbol{K}}\boldsymbol{q} = \boldsymbol{M}^{(-1/2)}\boldsymbol{B}\{\boldsymbol{f}\} \tag{5.9}$$

$\widetilde{\mathbf{K}}$ and $\widetilde{\mathbf{C}}$ are the mass-normalized stiffness and damping matrices, as illustrated in (5.10) and (5.11), respectively.

$$\widetilde{\boldsymbol{K}} = \boldsymbol{M}^{(-1/2)}\boldsymbol{K}\boldsymbol{M}^{(-1/2)} \tag{5.10}$$

$$\widetilde{\boldsymbol{C}} = \boldsymbol{M}^{(-1/2)}\boldsymbol{C}\boldsymbol{M}^{(-1/2)} \tag{5.11}$$

Additionally, to decompose the system into a modal coordinate representation, the coordinate **q** can be written in terms of the modal coordinate **r**, as shown in (5.12),

$$\boldsymbol{q} = \boldsymbol{P}\boldsymbol{r} \tag{5.12}$$

where **P** is the matrix of the orthonormal eigenvectors of $\widetilde{\mathbf{K}}$ and $\widetilde{\mathbf{C}}$ multiplied by the $\mathbf{P}^T$. The mass-normalized stiffness and damping matrices can be represented as shown in (5.13) and (5.14), respectively:

$$\boldsymbol{C_m} = \boldsymbol{P^T}\widetilde{\boldsymbol{C}}\boldsymbol{P} \tag{5.13}$$

$$\boldsymbol{\Lambda} = \boldsymbol{P^T}\widetilde{\boldsymbol{K}}\boldsymbol{P} \tag{5.14}$$

where $\mathbf{C_m}$ and $\boldsymbol{\Lambda}$ are the damping and stiffness matrices, for the modal coordinates. Finally, the equations of motion can be decomposed into the modal coordinate representation, as shown in (5.15).

$$\ddot{\boldsymbol{r}} + \boldsymbol{C_m}\dot{\boldsymbol{r}} + \boldsymbol{\Lambda}\boldsymbol{r} = \boldsymbol{P^T}\boldsymbol{M}^{(-1/2)}\boldsymbol{B}\{\boldsymbol{f}\} \tag{5.15}$$

The terms of the matrices are explicitly expressed in (5.16). After modal decomposition, for the proposed system, the stiffness and damping matrices are

diagonalized, and the significance is that it can be considered as three independent single-degree-of-freedom systems.

$$\begin{Bmatrix} \ddot{r}_{OCV} \\ \ddot{r}_{MT} \\ \ddot{r}_{DL} \end{Bmatrix} + \begin{bmatrix} c_{OCV} & 0 & 0 \\ 0 & 2\zeta_{MT}\omega_{n,MT} & 0 \\ 0 & 0 & 2\zeta_{DL}\omega_{n,DL} \end{bmatrix} \begin{Bmatrix} \dot{r}_{OCV} \\ \dot{r}_{MT} \\ \dot{r}_{DL} \end{Bmatrix} + \begin{bmatrix} 0 & 0 & 0 \\ 0 & (\omega_{n,MT})^2 & 0 \\ 0 & 0 & (\omega_{n,DL})^2 \end{bmatrix} \begin{Bmatrix} r_{OCV} \\ r_{MT} \\ r_{DL} \end{Bmatrix} = \begin{bmatrix} b_{OCV} \\ b_{MT} \\ b_{DL} \end{bmatrix} \{f\} \tag{5.16}$$

Figure 4.4 demonstrates the three-independent single-degree-of-freedom systems in modal representation. The significance of this transformation is that each mode can be considered individually to reflect the different dynamic effects of the battery.

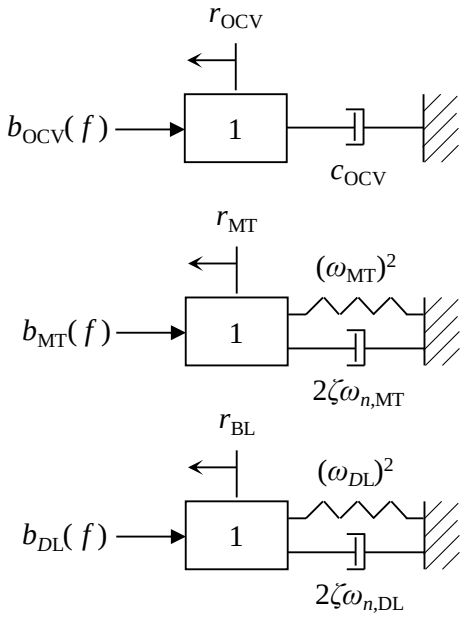

Figure 4.4: Spring-mass-damper system in modal representation

Here, r_{OCV} is the modal displacement, which represents the degradation of the open-circuit voltage. The natural frequency of this mode is zero rad/s which manifests as zero in the first diagonal term of the $\mathbf{\Lambda}$ matrix. Therefore, this is a rigid body mode that does not oscillate, and the open-circuit voltage never recovers after the current is drawn from the cell. The first diagonal term of the modal damping matrix is c_{ocv}, which limits the rate of change of the open-circuit voltage state, and stops the voltage drop when the cell is in equilibrium. Modes r_{MT} and r_{DL} represent the displacement of the mass transfer and double-layer degrees of freedom, respectively. The associated stiffness terms are the squared natural frequencies $\omega_{n,\mathrm{MT}}$ and $\omega_{n,\mathrm{DL}}$ and, which dictate the rate at which each mode responds.

By convention, the natural frequencies are ordered as the lowest first and the highest last. Therefore, the rigid-body mode is the first mode. The mass transfer phenomenon is known in electrochemistry to dominate the lower-frequency dynamics of batteries. Therefore, $\omega_{n,\mathrm{MT}}$ are in second order. Similarly, the double-layer phenomenon is associated with higher-frequency dynamics. Accordingly, $\omega_{n,\mathrm{DL}}$ are in the third order. Subsequently, these frequency-range dependencies are significant in the transient time responses.

Furthermore, the corresponding terms in the damping matrix are expressed in a standard form in relation to the natural and nondimensionalized damping ratios. The damping ratio dictates the relative rate at which each oscillation mode decays over time. The input force, which was assumed to only act upon m_1, contributed to

the excitation of all three modes according to the modally transformed input matrix **B**. The gains of the input matrix become b_{OCV}, b_{MT} and b_{DL} which are the amounts at which the single input current affects each mode. The system in modal coordinates is shown graphically in the block diagram in Figure 4.5. Each mode, which is the SISO single-degree-of-freedom, is indicated by a dashed rectangular box. In general, the r_{MT} signal is associated with a lower dynamic frequency component, and the r_{DL} signal is associated with a dynamic higher frequency component. The output signal V_{out} is a modal summation containing all frequency components. The input to the system was the current at which the battery was discharged. V_{out} is the voltage measured across the battery terminals. Furthermore, V_{OCV} is an internal signal related to the SOC.

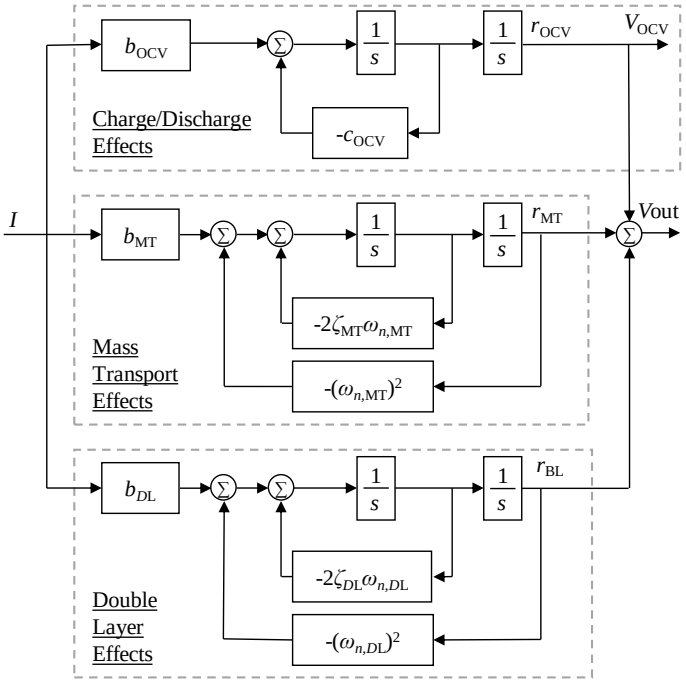

Figure 4.5: Block diagram of the battery dynamic analog

The purpose and unique benefits of this mechanical system are to accurately predict the runtime, steady state and transient response of the battery. In addition, the model has the capability to numerically quantify and graphically display the effects that the mass transfer and double layer has on the battery for the entire SOC range, which were previously evaluated at a fixed SOC. Finally, the model can predict the nonlinear SOC-OCV relationship.

4.1.2. Lumped Thermal Model

The lumped thermal model presented in this section is utilized to predict the thermal behavior of cylindrical batteries since it has a uniform temperature distribution along its surface. For a body to be considered as a lumped system, the Biot number criteria expressed in (5.17) was confirmed.

$$Bi = \frac{hD}{k_b} \leq 0.1 \tag{5.15}$$

Here, D and k_b are the diameter and the thermal conductivity of the battery. Additionally, h is convection the heat transfer coefficient obtained from the natural convection equations of Nusselt number, which is a function of the Rayleigh and Prandtl numbers [56]. Here, the heat transfer coefficient is function of the surface temperature for a specific geometry. The Nusselt number equations for a horizontal cylinder are given by (5.16) - (5.17):

$$Nu = \frac{hD}{k_f} \tag{5.16}$$

$$Nu = \left\{ 0.6 + \frac{0.387 Ra_D^{\frac{1}{6}}}{[1 + (0.559/Pr)^{\frac{9}{16}}]^{\frac{8}{27}}} \right\}^2 \tag{5.17}$$

From (5.17), Ra_D is Rayleigh number which describes the relationship between buoyancy and viscosity in the fluid and *Pr* is Prandtl number which establishes the relationship between the momentum diffusivity and thermal diffusivity. Moreover, the Rayleigh number is obtained through (5.18),

$$Ra_D = \frac{g\beta(T - T_{amb})L_c^3}{v^2} Pr \tag{5.18}$$

where g is the gravitational acceleration, β is the coefficient expansion, L_c is the characteristic length of the geometry and *v* is the kinematic viscosity. Furthermore, the energy balance equation of a single cell can be expressed as shown in (5.19).

$$\rho V C_p \frac{dT}{dt} = \dot{Q}_{ECh} + \dot{Q}_{conv} + \dot{Q}_{rad} \tag{5.19}$$

Where ρ is the density of the battery, C_p is the heat capacity, V is the volume and T is the temperature. Furthermore, $\dot{Q}_{ECh}$ is the heat power generated from the battery due to the overpotential and entropic heating. Bernardi *et al.* [57] established this term as displayed in (5.20).

$$\dot{Q}_{ECh} = I(V - V_{OCV}) + IT \frac{\partial V_{OCV}}{\partial T} \tag{5.20}$$

This expression neglects the uneven heat generation and phase change heat generation of the battery reactants. For further simplification, the entropic heating was neglected [58].

Furthermore, $\dot{Q}_{conv}$ is the convection heat transfer term and is defined through (5.21), where A is the surface area of the battery and T_{amb} is the ambient temperature.

$$\dot{Q}_{conv} = hA(T - T_{amb}) \tag{5.22}$$

Additionally, the last term from (5.19) incorporates the heat transfer due to radiation effects. $\dot{Q}_{rad}$ is defined through (5.23), where ε is the emissivity constant and was set to 0.80 [40] and σ is Stefan-Boltzmann's constant equivalent to 5.67×10^{-8}.

$$\dot{Q}_{rad} = \varepsilon\sigma A\left(T^4 - {T_{amb}}^4\right) \tag{5.23}$$

4.1.3. Transient Thermal Model

The surface temperature for a pouch cell is non-uniform; therefore, it cannot be considered a lumped thermal body. To formulate a model capable of estimating the temperature profile and contour of a pouch cell, two-dimensional conduction must be considered. The model developed in this section presents a two-dimensional transient thermal system based on numerical methods. The system is utilized to predict the surface temperature of a pouch cell at different locations along its surface. Numerical methods for solving differential equations such as the finite difference method are based on replacing the differential equations with algebraic

equations, which is accomplished by replacing derivatives by differences. The surface temperature of the battery was estimated by solving the energy balance at discrete points known as nodal points or nodes. Figure 4.6 illustrates the zones at which the pouch cell was split into control volumes to formulate the finite difference method system of equations.

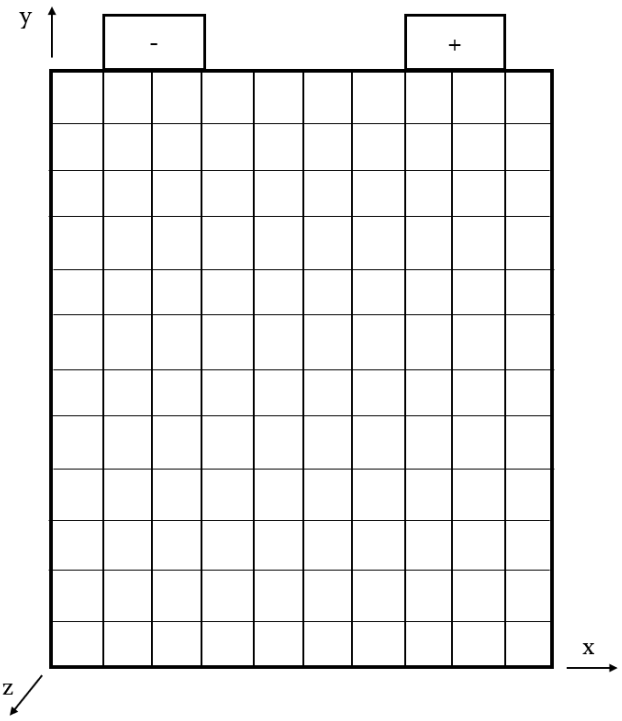

Figure 4.6: Pouch cell finite difference model

The characteristics equation of the system is illustrated in (5.24). Where, $\dot{Q}_{j,cond}$ is conduction in the y-axis, $\dot{Q}_{i,cond}$ is conduction in the x-axis, and $\dot{Q}_{tab}$ is the heat generated from the tabs. Additionally, Δx and Δy are the size of the element in the mesh.

$$\rho\Delta x\Delta y c_p \frac{T_{i,j}^{i+1} - T_{i.j}}{\Delta t} = \dot{Q}_{j,cond} + \dot{Q}_{i,cond} + \Delta y\left[\dot{Q}_{conv} + \dot{Q}_{rad}\right] + \Delta x\left[\dot{Q}_{conv} + \dot{Q}_{rad}\right] + \Delta x\Delta y\left[\dot{Q}_{conv} + \dot{Q}_{rad}\right] + \Delta x\Delta y\left[\dot{Q}_{ECh} + \dot{Q}_{tab}\right] \quad (5.24)$$

The equation describes the conduction between the node points, the convection and radiation from the top, side, and normal to the surface of the battery. Additionally, the heat generated from the battery and the tab while discharging. Moreover, the equation is solved at nodal point at the different control volume along the surface of the battery simultaneously. The equation presented in (5.24) is the overall energy balance; therefore, different thermal effects occur at different control volumes. For instance, the heat generated through the tabs does not affect control volume 11 directly, hence, that term goes to zero when solving for the temperatures in that volume.

The conduction heat transfer in the x-axis is expressed through (5.25).

$$\dot{Q}_{i,cond} = k\Delta y \frac{T_{i-1} + T_{ij}}{\Delta x} \quad (5.25)$$

Where, k is the conduction heat transfer coefficient, which is a material property. Conduction in the y-axis is analogous to that in the x-axis.

Additionally, the heat generated through the tabs of the battery can be conveyed through (5.26).

$$\dot{Q}_{tab} = \left(\frac{I}{L_{tab}W_{tab}}\right)^2 \left(\frac{1}{\sigma_{tab}}\right) \quad (5.26)$$

Where, W_{tab} and L_{tab} are the width and length of the tab, and σ_{tab} is the electrical conductivity of the tab material.

Additionally, the heat transfer coefficient was obtained through the natural convection relationship of Nusselt number, Rayleigh and Prandtl numbers as illustrated for the lump thermal model in section 4.1.2. Equation (5.27) displays the Nusselt number for a vertical plate [56].

$$Nu = \left\{ 0.825 + \frac{0.387 Ra_D^{\frac{1}{6}}}{[1 + (0.492/Pr)^{\frac{9}{16}}]^{\frac{8}{27}}} \right\}^2 \tag{5.27}$$

Furthermore, the equations were solved explicitly; therefore, the timestep Δt, is limited by the stability criterion. If the timestep is sufficiently small, the solution will diverge from the actual solution and become unstable. Additionally, a violation of the stability criterion will result in the violation of the second law of thermodynamics [56]. For a transient two-dimensional conduction heat transfer in rectangular coordinates, the stability criterion is expressed through (5.28).

$$\Delta t = \frac{\alpha \tau}{l^2} \leq \frac{1}{4} \tag{5.28}$$

Where, τ is the mesh Fourier number, α is the thermal diffusivity of the material and $\Delta x = \Delta y = l$.

Chapter 5 Thermo-Mechanical Battery Model Validation

5.1. Introduction

This section presents simulation results obtained from the dynamic system and the thermal models for four lithium-ion batteries, three cylindrical cells and one pouch cell. The dynamic model is utilized to match the terminal voltage and predict the OCV. Furthermore, the electrochemical heat generation computed from the OCV, and the terminal voltage was used as an input to the thermal models to obtain the temperature profile of each battery.

The parameters of the proposed modal battery model were numerically tuned for the four lithium-ion cells. The parameters of the modal decomposed battery model are listed in Table 5.1. As shown in the table, the parameters were tuned as a function of the SOC. To improve the fitment of the simulation results, the parameters were optimized by employing the method of nonlinear least squares via the Trust-Region-Reflective algorithm. This was accomplished using the parameter estimation toolbox in MATLAB Simulink. Each parameter was tuned as a lookup table in terms of the SOC as 20 discrete values from 0.05 to 1.

The damping ratios were constrained to be greater than unity because all the transient behaviors were observed to be overdamped. In addition to that, the modal

input gains were allowed to take any positive value. However, the initial C_{OCV} range was not known; it was found by iterating that an upper bound is required to achieve the optimizer convergence.

Table 5.1: Modal battery parameters

Symbol	Description	Units
c_{OCV} (SOC)	Rigid body mode damper	rad/s
$\omega_{n,MT}$ (SOC)	Mass transfer natural frequency	rad/s
$\omega_{n,DL}$(SOC)	Double layer natural frequency	rad/s
ζ_{MT} (SOC)	Mass transfer damping ratio	-
ζ_{DL} (SOC)	Double layer damping ratio	-
b_{OCV} (SOC)	Rigid body mode input gain	rad/Ns²
b_{MT} (SOC)	Mass transfer input gain	rad/Ns²
b_{DL} (SOC)	Double layer input gain	rad/Ns²

To tune the parameters accurately and obtain a model that represents the physical dynamics of the battery, the natural frequency values were limited to the maximum and minimum values according to the angular frequency values typically observed in electrochemical cells, as reported in the literature. Table 5.2 shows the angular frequency values obtained experimentally via the electrochemical impedance method for batteries [59].

Table 5.2: Typical angular frequency values for Li-ion batteries

Parameter	Effect	Range (rad/s)
$\omega_{n,EM}$	Electric & Magnetic	$105 - 6.3\times10^{6}$
$\omega_{n,BL}$	Double layer	0.1 - 10000
$\omega_{n,MT}$	Mass transfer	$0.09\text{x}10^{-3} - 12.5$
$\omega_{n,C}$	Cycling, SOC	$4\times10^{-6} - 7\times10^{-4}$
$\omega_{n,RE}$	Reversible	$2\times10^{-7} - 3\times10^{-4}$
$\omega_{n,AE}$	Aging	$6.2\times10^{-8} - 2\times10^{-6}$

The convection heat transfer coefficient was estimated utilizing the Nusselt number relationships shown in (5.16) - (5.18). The value was optimized as a function of the temperature change independent of the dynamic model tuning. Initially, the density and specific heat of the battery were estimated by computing the summation of the assumed materials in the cell core (anode, cathode, and separator), the positive and negative tab materials and the insulation film as reported in literature for cylindrical and pouch batteries [37]. These values were also optimized as a function of temperature and updated for the entire experimental history. The next four subsections cover the results of voltage and temperature responses estimated by the coupled model and discusses the signals extracted from the model to characterize the batteries considered.

5.2. Cylindrical Cells

5.2.1. Samsung INR 1850-25R

From the load cycle data illustrated in Figure 3.5 for the discharge rates of 1C and 2C, the SOC was computed utilizing the coulomb counting expressed in equation (2.8). Shown in Figure 5.1 are the SOC trajectory for the 1c discharge. Note that the 1C discharge is only during on pulses.

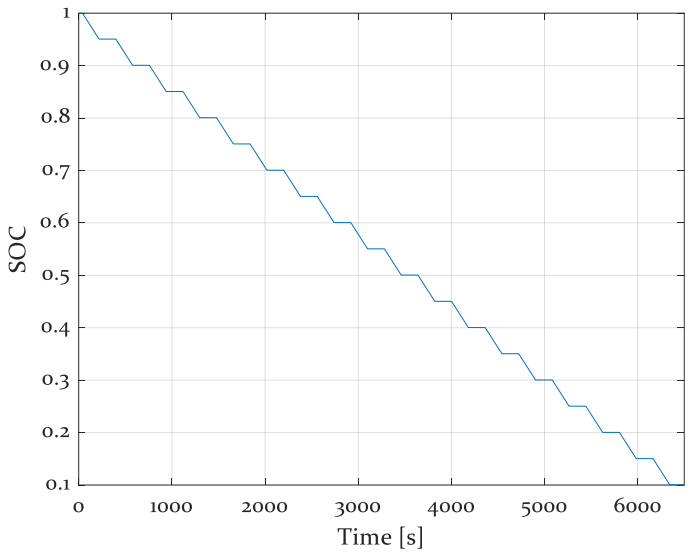

Figure 5.1: Samsung INR-18650 1C SOC trajectory

The SOC of the battery began at 100% and decreased with each current pulse. The battery is almost fully discharged; therefore, the modal parameters can be optimized for nearly the entire SOC range. From the computed SOC, the modal parameters were then tuned as a function of SOC from 1C discharge HPPC test and validated from the data for the 2C HPPC test. Once the parameters have been optimized, the

system was then simulated using the experimental current draw as the input. Figure 5.2 shows the experimental terminal voltage and the simulated system response of the modally decoupled coordinates over the same time history.

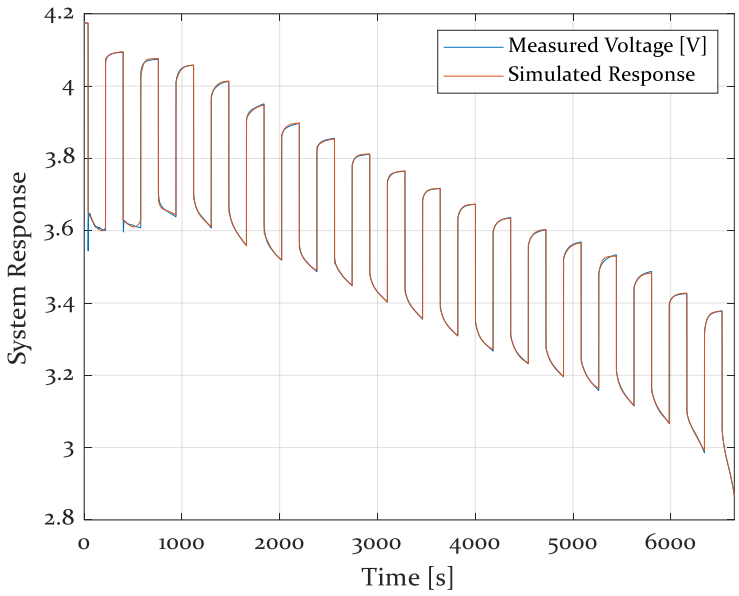

(a)

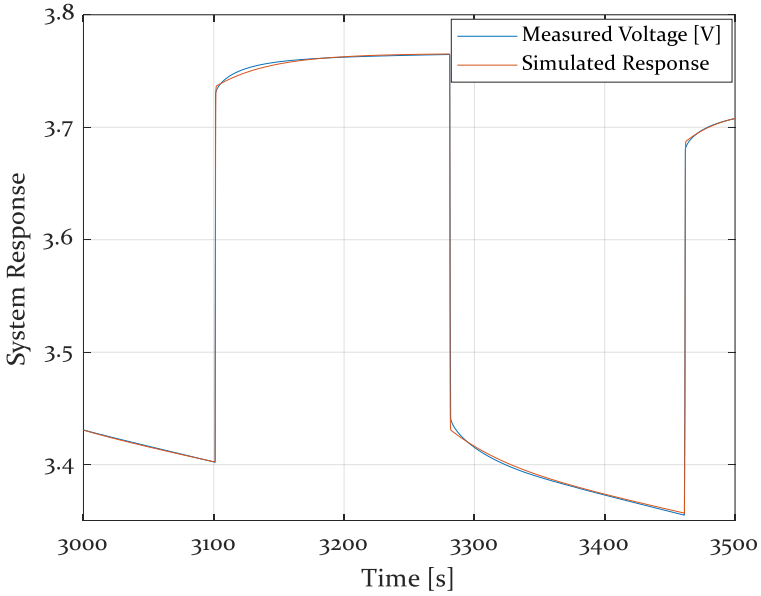

(b)

Figure 5.2: Samsung INR 1860-25R 1C estimated voltage response relative to measured voltage.

Additionally, to further elaborate on how the simulated results were fitted to the experimental voltage and predict the nonlinear dynamics of the battery, Figure 5.2 *(b)* displays a rescaled plot of the experimental voltage relative to that estimated by the mechanical analogy system that occurred during the time interval 3000s ≤ t ≤ 3500s. The dynamic model utilized in this study was able to match the voltage response of the battery within 0.41% standard deviation error.

Moreover, Figure 5.3 displays the predicted by the modal signal V_{OCV}, relative to the electrical potential measured at the peaks of the relaxation period. Again, the dynamic model estimated the OCV of the battery within high level of accuracy; therefore, the model can be used to estimate OCV and to compute the overpotential heat generation rate.

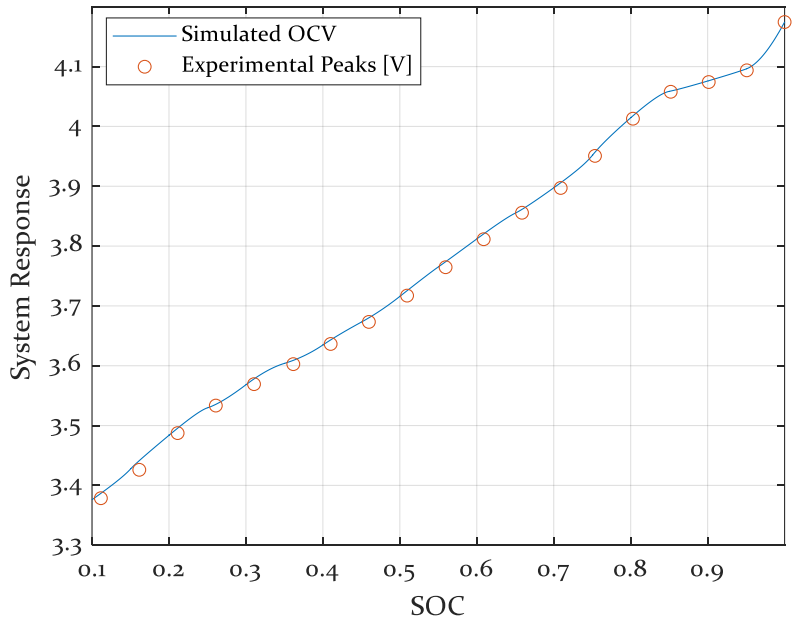

Figure 5.3: Samsung INR 18650-25R OCV estimation

Furthermore, Figure 5.4 shows the displacement signals r_{MT} and r_{DL}, which correspond to the mass transfer and double-layer effects, which are internal to the battery model. As expected, the higher natural frequency mode, which corresponds to the double-layer effect, dominates the instantaneous drop and recovery periods in the battery voltage. This effect is caused by the charge layer formed between the electrode and electrolyte, which resembles the behavior of a capacitor.

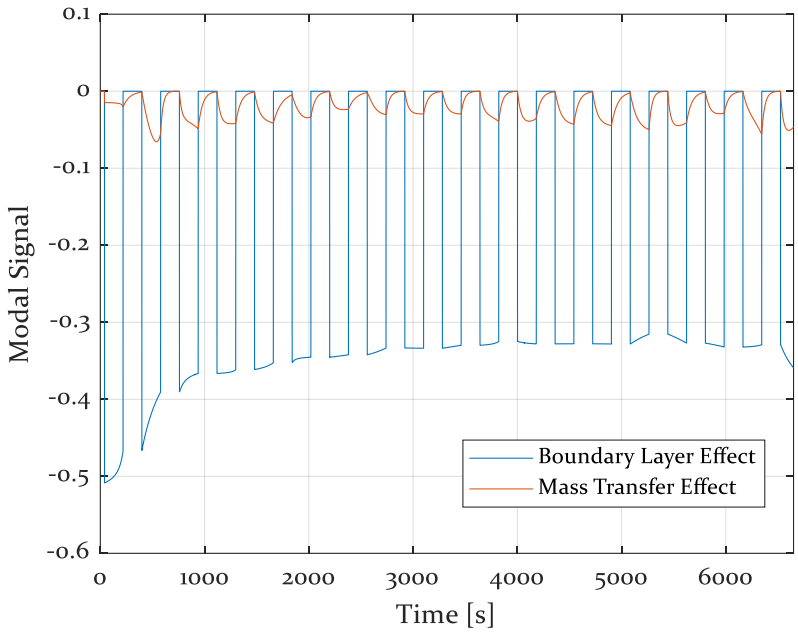

Figure 5.4: Samsung INR 18650-25R boundary layer and mass transfer effects

From the OCV and the terminal voltage estimated by the dynamic model, the over potential heat generated by the battery was calculated, as illustrated in Figure 5.5. The heat generation is then used to predict the battery temperature by coupling the dynamic model with the lumped thermal system and compared with experimental data, as shown in Figure 5.6.

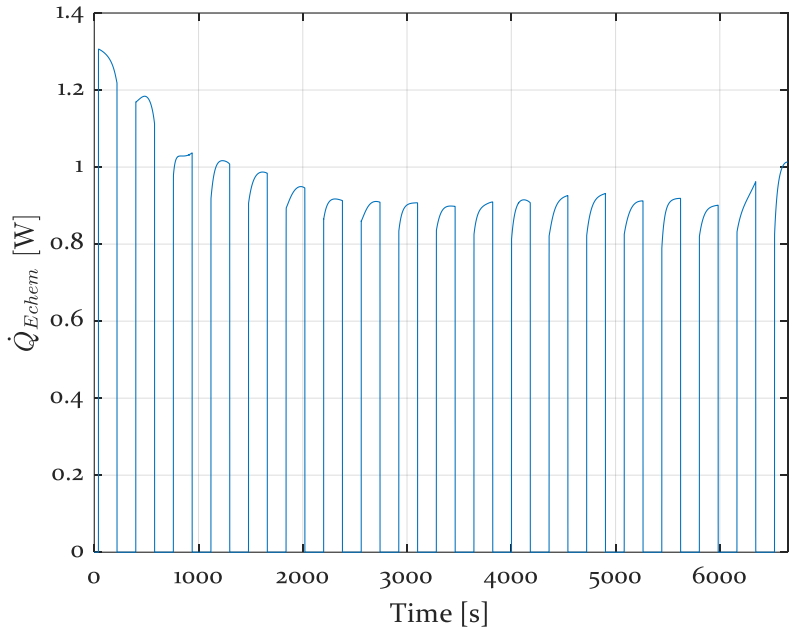

Figure 5.5: Samsung INR18650 – 25R 1C over potential heat generation

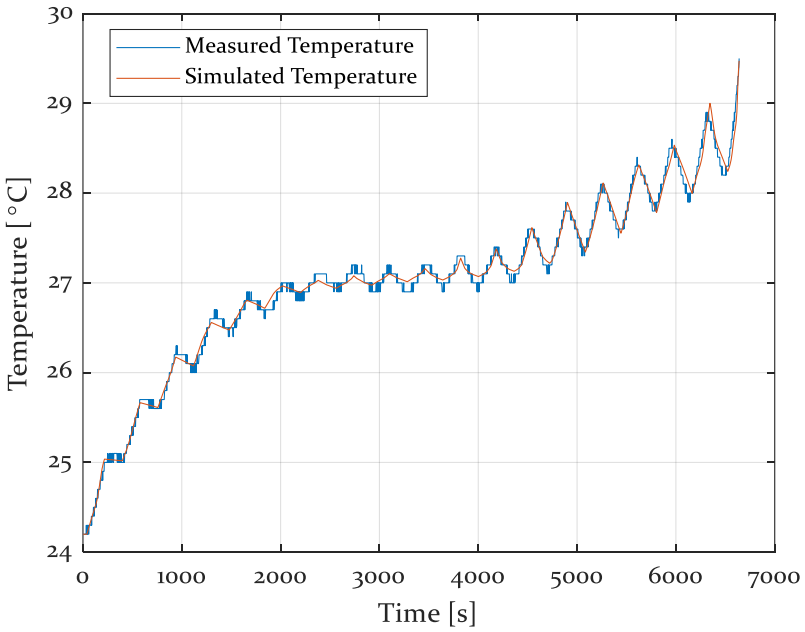

Figure 5.6: Samsung INR 18650 – 25R temperature estimated compared to measured

The model estimated the surface temperature of the battery within 0.16% standard deviation of the error. Moreover, the temperature increases with each current pulse

due to the heat generation signal. The overall temperature rises to steady-state at around 27°C and after approximately 4000s, the temperature due to the changing model parameters at low SOC.

Furthermore, the optimized modally decomposed parameters were validated by carrying out the HPPC test at 2C and evaluating the fitment of the voltage response. Shown in Figure 5.7 is the SOC estimation for the 2C discharge rate.

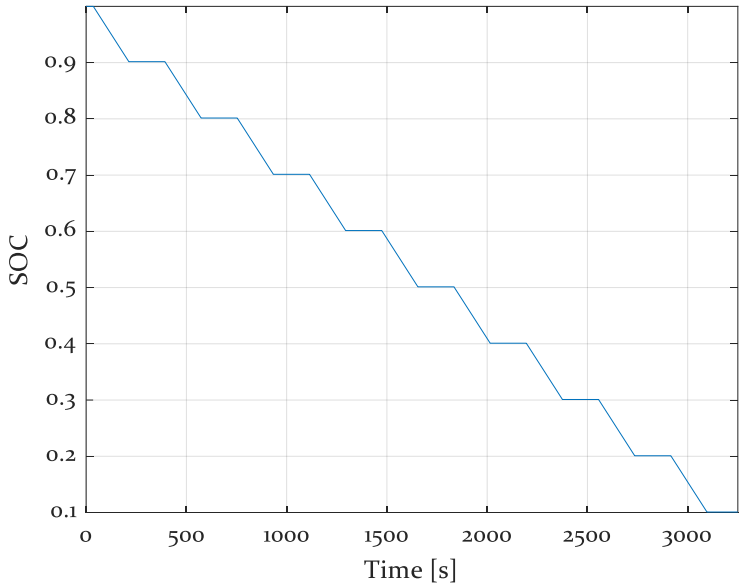

Figure 5.7: Samsung INR 18650- 25R 2C SOC trajectory

Correspondingly in Figure 5.8 is the simulate voltage response of the battery related to that measured experimentally.

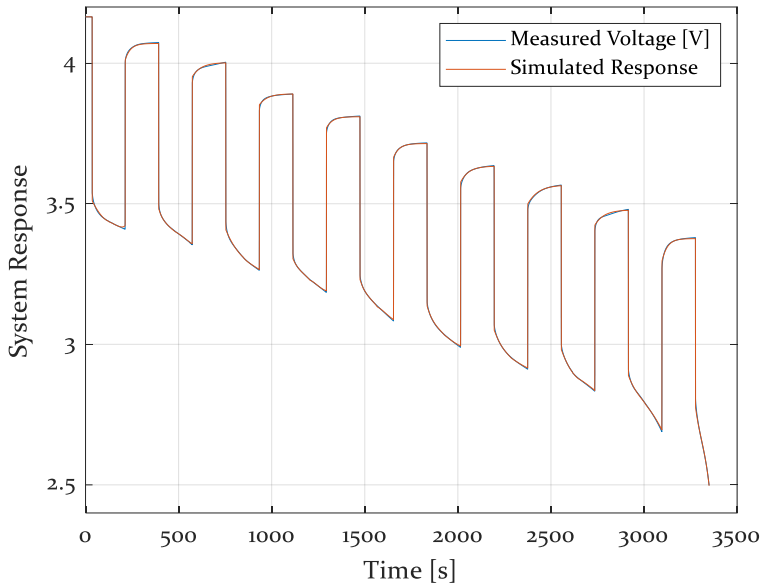

(a)

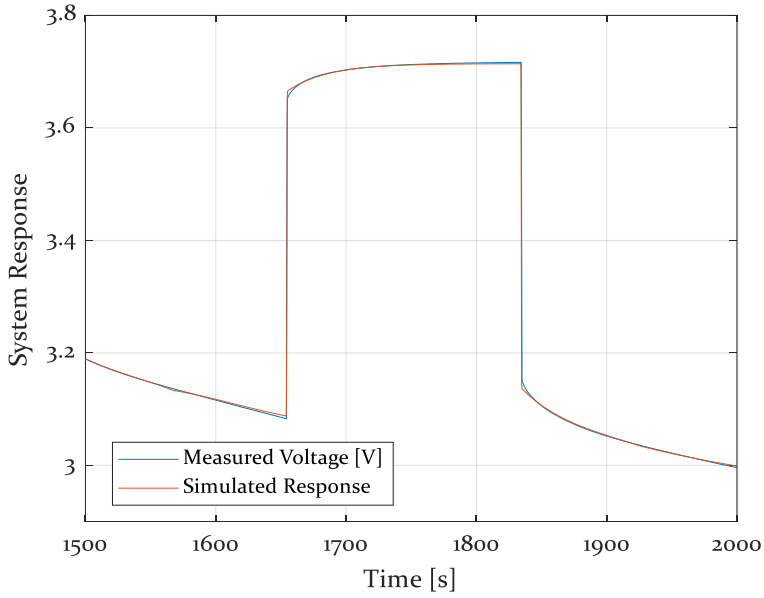

(b)

Figure 5.8: Samsung INR 18650-25R 2C voltage response

The simulated response fit the measured within 0.82% standard deviation of the error. Moreover, the OCV was also validated as shown in Figure 5.9, as the model estimated the OCV within a high level of accuracy.

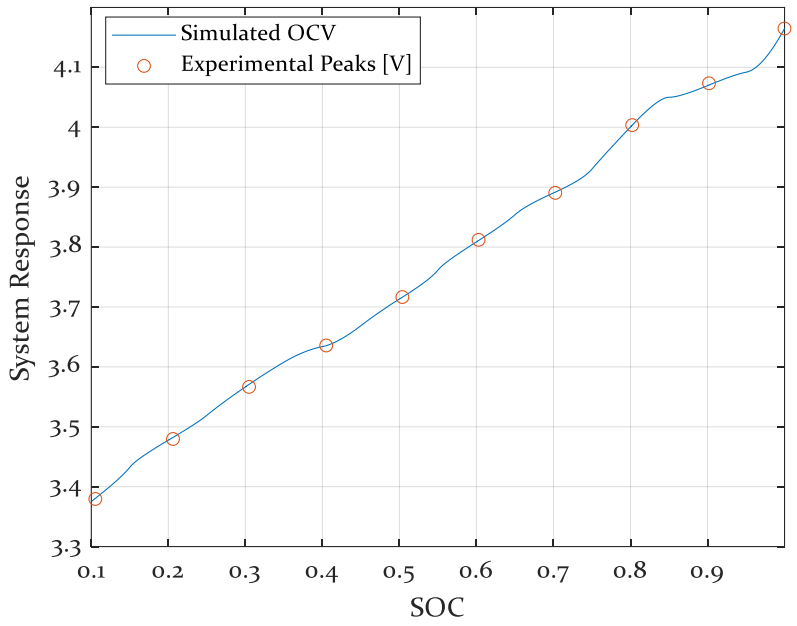

Figure 5.9: Samsung INR 18650 – 25R 2C OCV estimation

From the terminal voltage and the OCV, the overpotential heat generated was computed as shown in Figure 5.10.

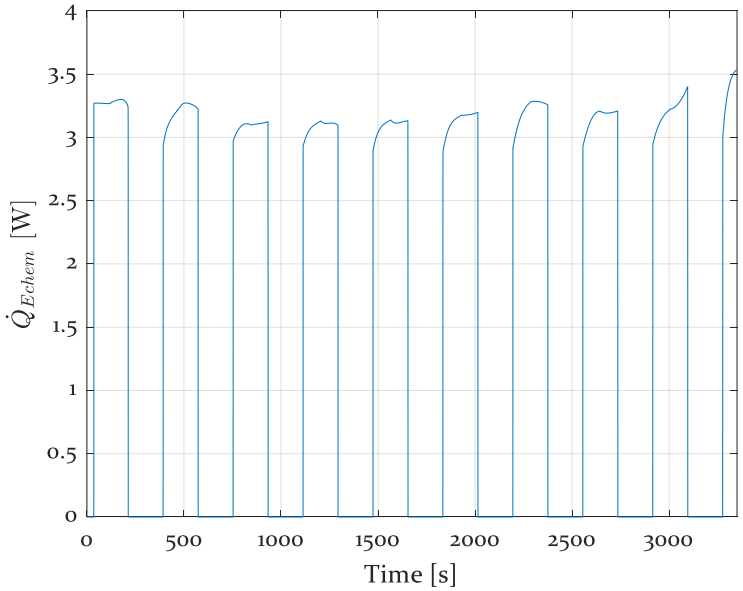

Figure 5.10: Samsung INR 18650 – 25R 2C overpotential heat generation

Finally, the overpotential heat generation is used as an input to the lumped thermal model to estimate the temperature profile along the surface of the battery. The model was able to estimate the surface temperature of the battery within 0.25% standard deviation of the error, as shown in Figure 5.11.

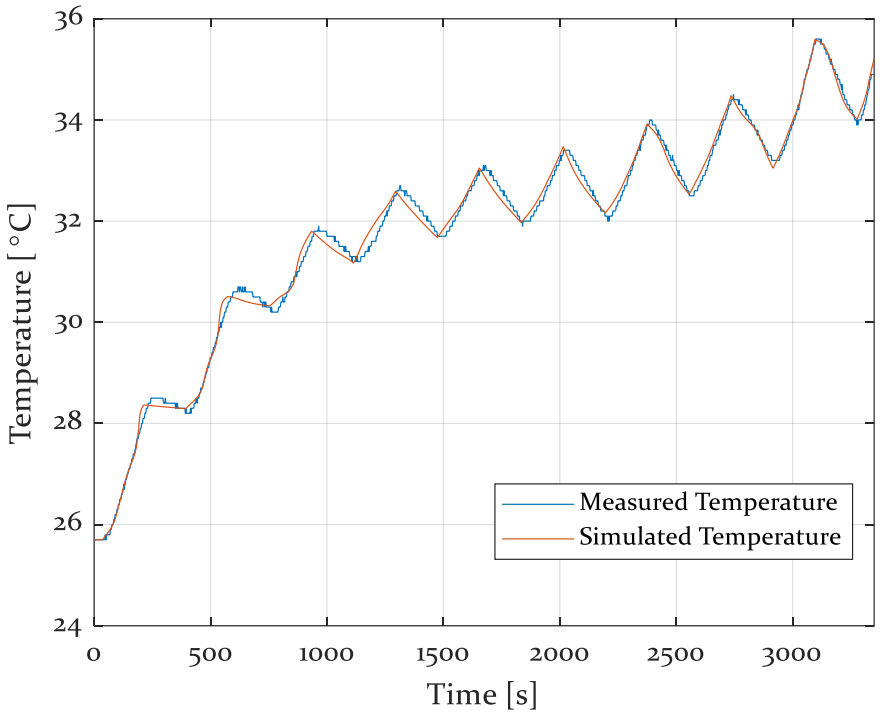

Figure 5.11: Samsung INR 18650 – 25R 2C temperature estimation

5.2.2. Panasonic NCR 27100

The same analysis was carried out on the Panasonic NCR 27100. The main purpose of this analysis was to validate the accuracy of the model on cells with different form factors and chemistries.

Furthermore, from the measured current data illustrated in Figure 3.6, the SOC for both discharge rates were computed, as shown in

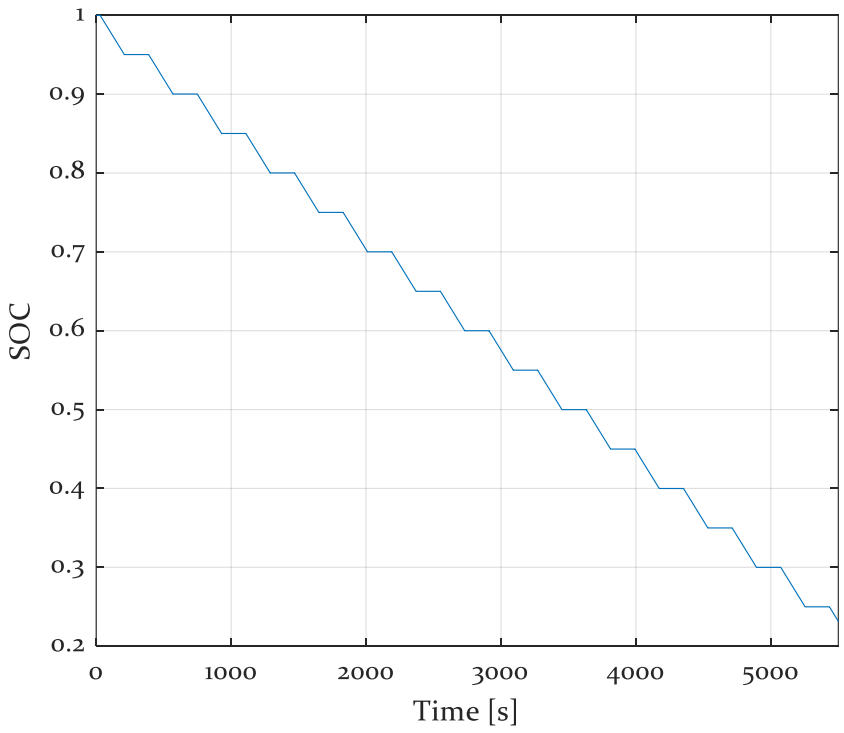

(a)

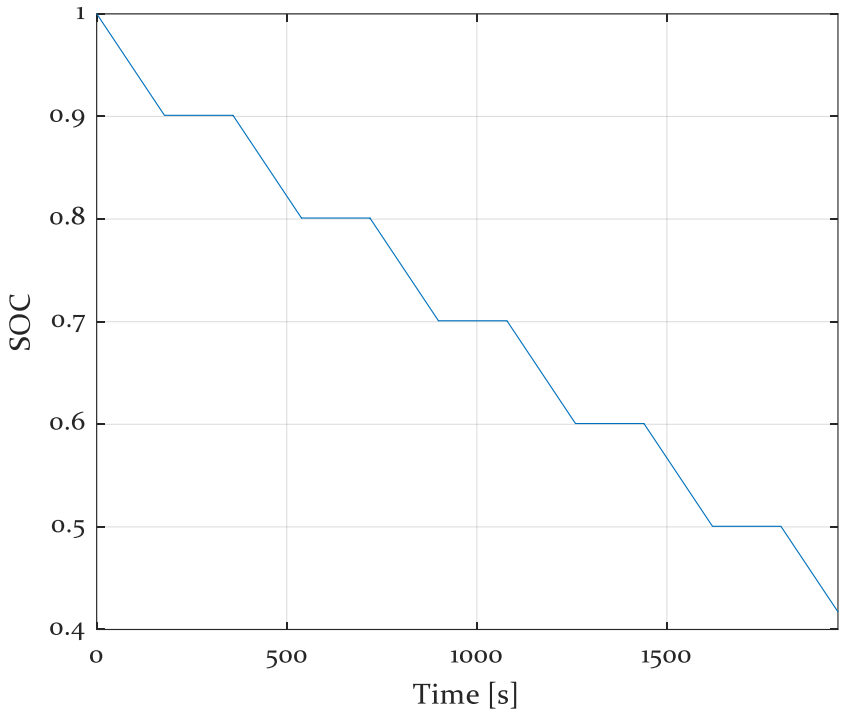

(b)

Figure 5.12: Panasonic NC 21700 SOC

The SOC of the battery began fully charged with an SOC of 1 and decreased by 0.05 after each current pulse at 1C, whereas at 2C, the SOC decreased by 0.1 over each pulse. The modal parameters were then fit as a function of this SOC computed to fit the corresponding experimentally measured battery terminal voltage.

Figure 5.13 displays the battery terminal voltage as predicted by the dynamic model compared to the measured terminal voltage. With each pulse of current, the electrical potential drops mainly due to the mass transfer effect and double-layer effect degrees of freedom, and when the current load is set to zero, most of the electrical potential is recovered from the vibration of these modes. However, a slight portion of the voltage is lost due to the static-discharge mode.

To statistically evaluate the fitment of the dynamic model to the measured terminal voltage, the error standard deviation was computed. It was found that the model was able to match the voltage response of the battery within 0.96% and 2.15% of standard deviation of the error, for the 1C and 2C discharge rates, respectively.

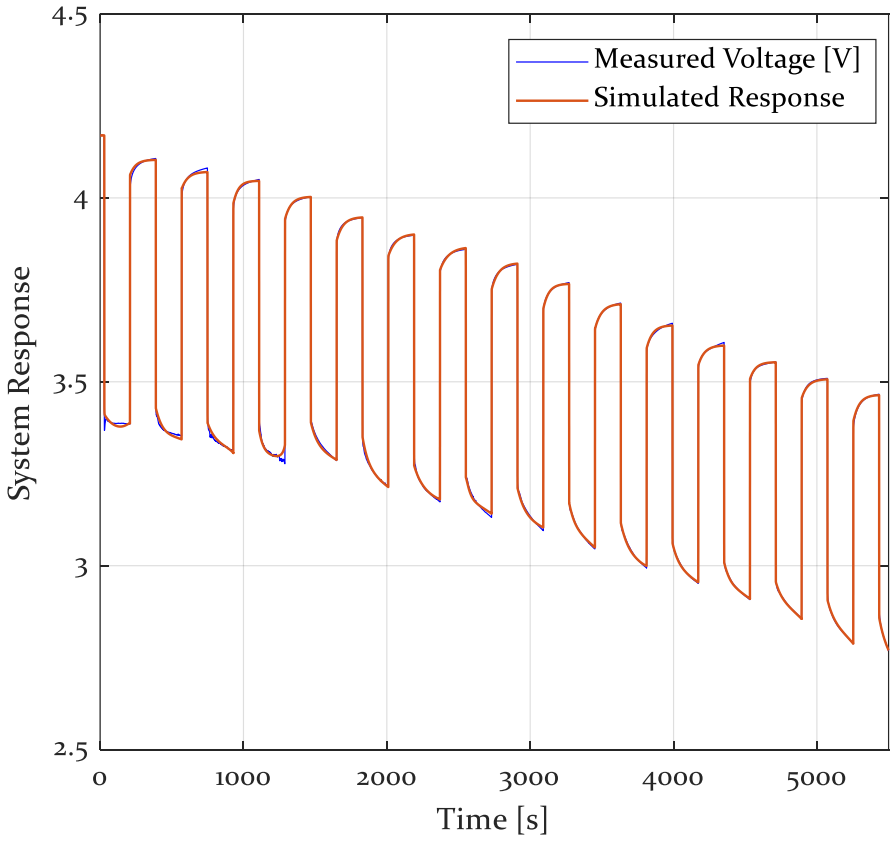

(a)

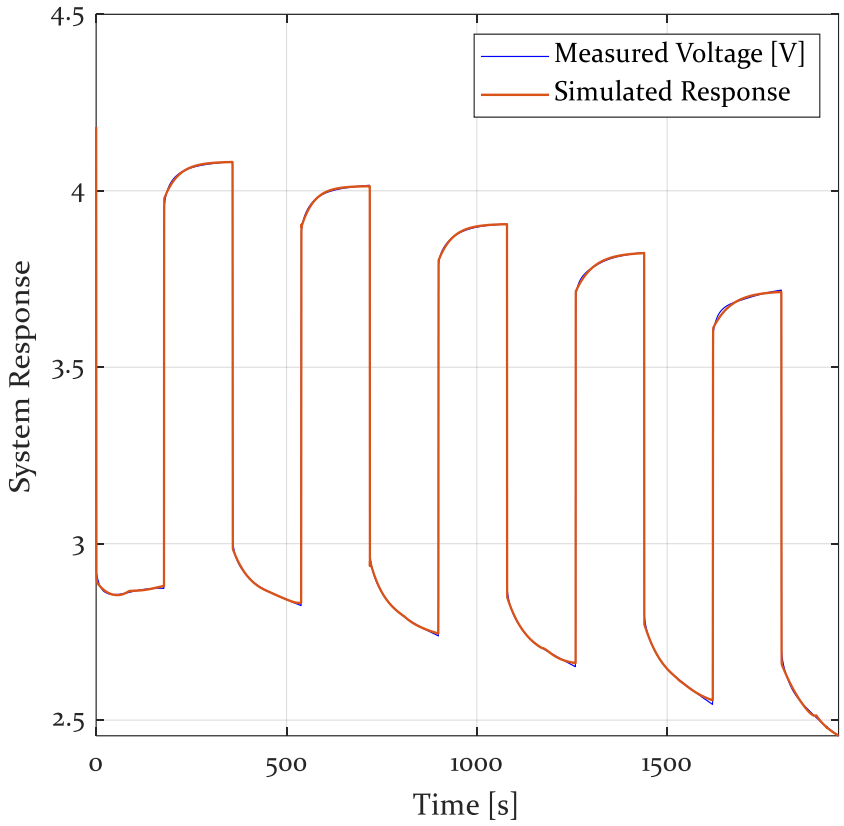

(b)

Figure 5.13: Panasonic NCR 27100 voltage estimation

The OCV predicted by the steady-state component of the experimental data and the mode signal V_{OCV} are shown in Figure 5.14. The experimentally based OCV was found by taking the peak voltage value during the regeneration period relative to the SOC. This neglects any small remaining transient to steady-state due to the frequency and duty cycle that induced the current load. In general, good agreement is found; therefore, it can be deemed apt to use the predicted parameters from the model to estimate the heat energy generated by the battery.

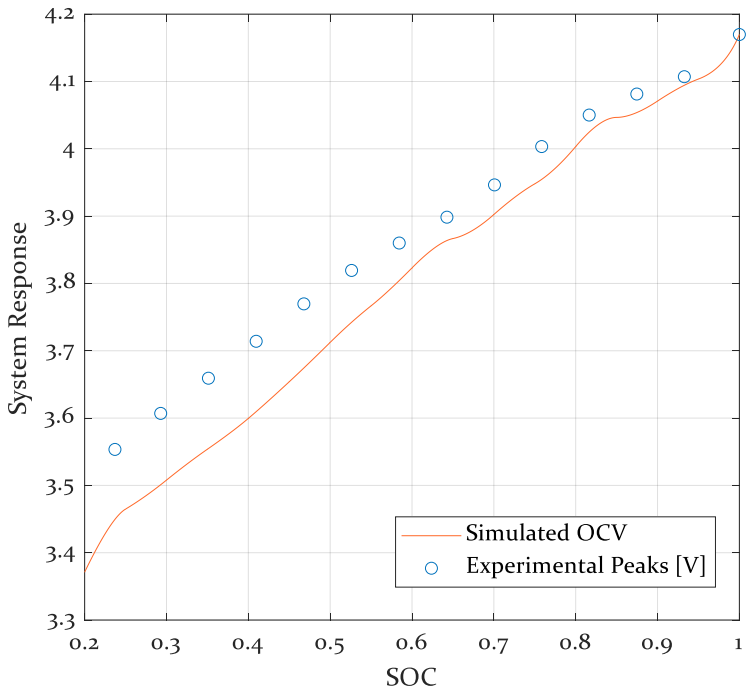

(a)

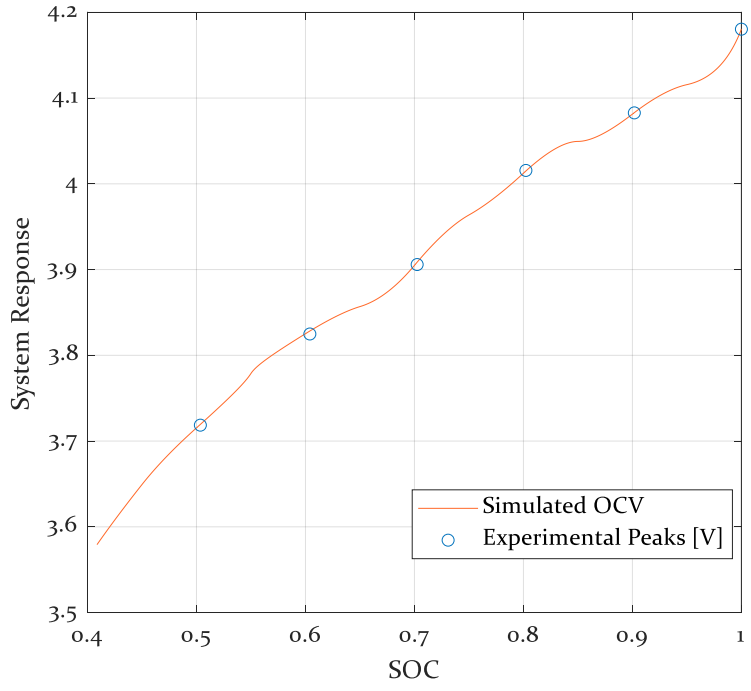

(b)

Figure 5.14: Panasonic NCR 21700 OCV estimation

Good agreement is found between the OCV predicted as a state within the dynamic model and that from the quasi-static component of the experiment. With the terminal voltage and OCV estimated, the overpotential heat generation was computed for both discharge rates.

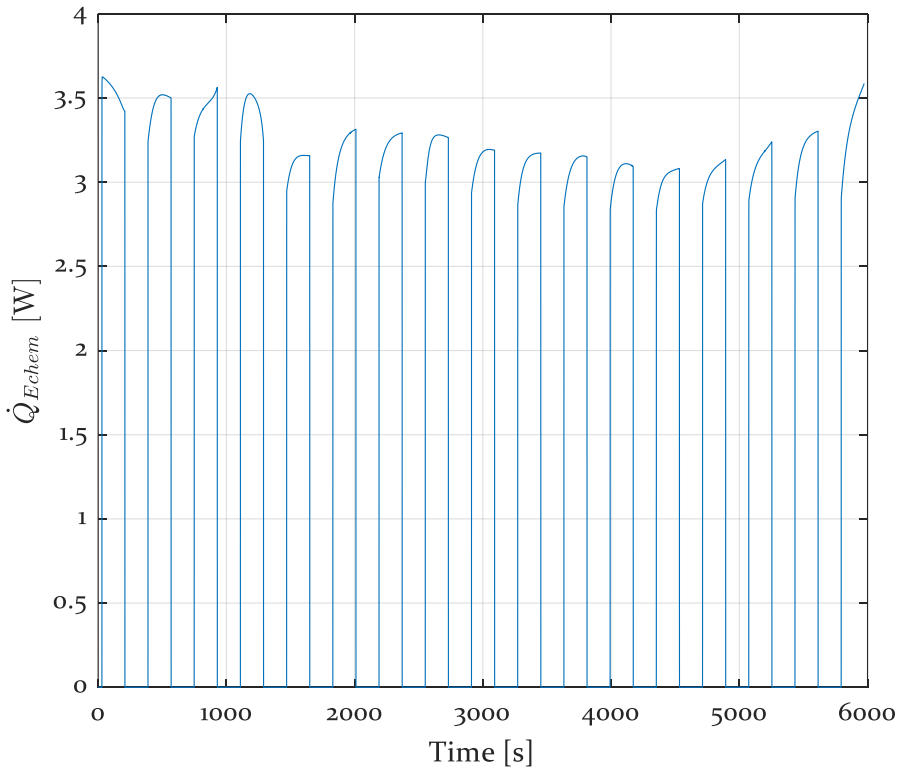

(a)

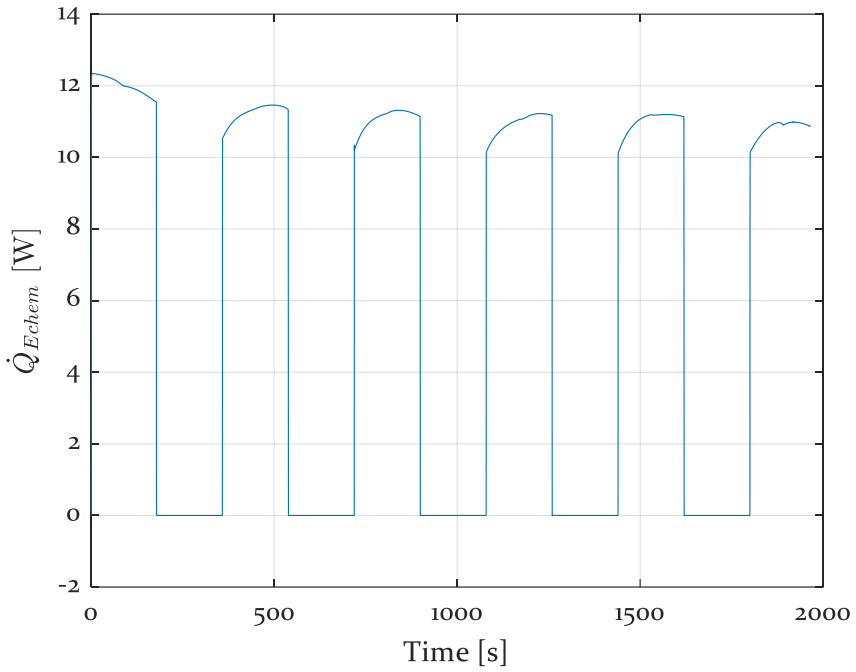

(b)

Figure 5.15: Panasonic NCR 21700 overpotential heat generation

With each current pulse, heat is generated from the battery due to the electrochemical reactions the battery undergoes as being discharged. On average, the overpotential power generated by the battery increased by 70.62% when discharged at 2C relative to 1C.

Then, the estimated heat generation history is used to predict the surface temperature profile of the battery over time. Figure 5.16 displays the temperature response measured experimentally relative to that predicted by the lumped thermal model for both discharge rates. The higher discharge rate results in the battery reaching a higher temperature in keeping with the greater heat generated.

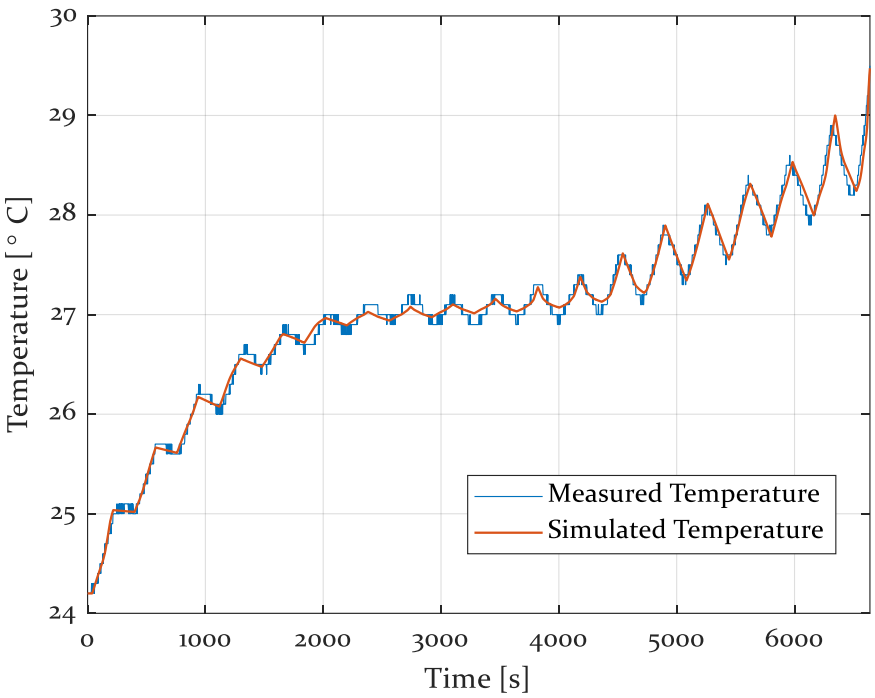

(a)

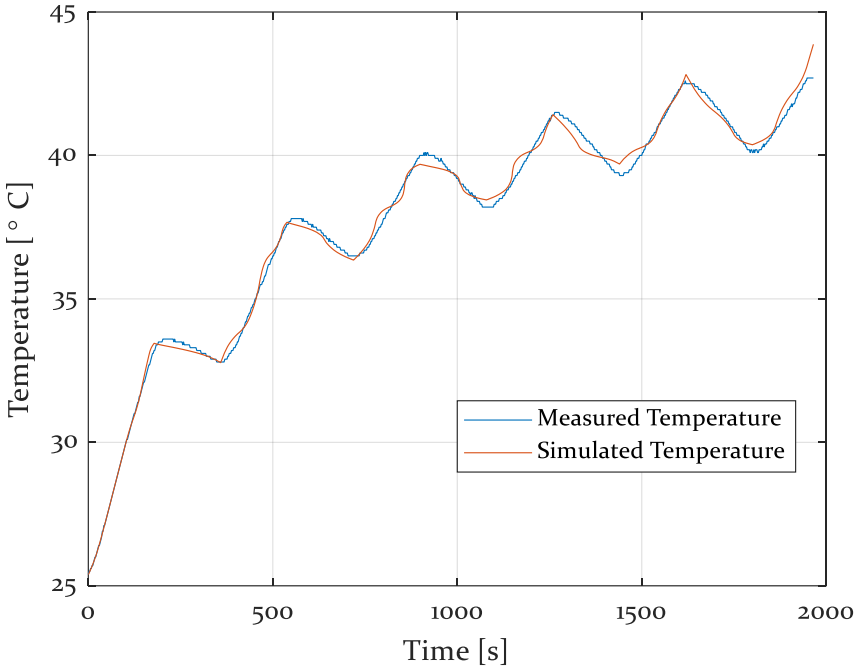

(b)

Figure 5.16: Panasonic NCR 27100 temperature estimation

5.2.3. Samsung INR 18650-20R

This section presents the data obtained from the CALCE battery research team [51]. The datasets were used to compare the results obtained by Zhang et al. [22] to the proposed model's simulated response. As mentioned, two datasets were utilized. The first dataset was used to estimate and identify the modal parameters and the second dataset was used to validate the identified parameters. For the incremental current OCV test, the battery was pulsed with 1A for 12 minutes and allowed to recover for 2 hours to reach steady state as shown in Figure 3.8. With the SOC computed and the current load utilized as the input force to the system, the modal parameters were tuned and optimized to fit the measured terminal voltage obtained experimentally. Figure 5.17 (a) displays the simulated model system response in contrast to the measured terminal voltage for the overall discharge period. Figure 5.17 (b) displays a rescaled plot for the pulses that occurred during the time interval of $30000s \leq t \leq 55000s$. Additionally, As displayed in the figures, the system response of the proposed model had the capability to match the measured terminal voltage with a 1.03% standard deviation error, which indicates the high level of precision of the model.

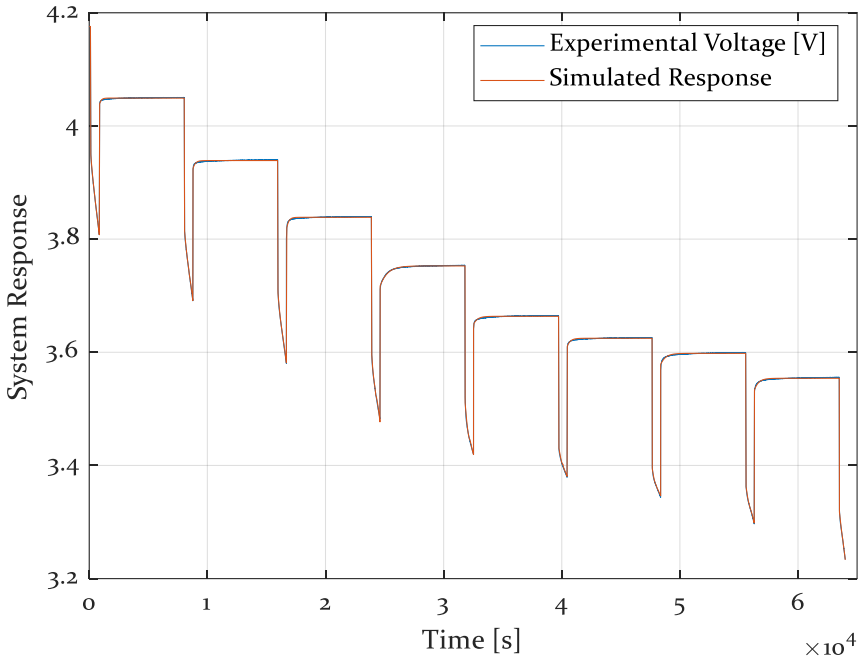

(a)

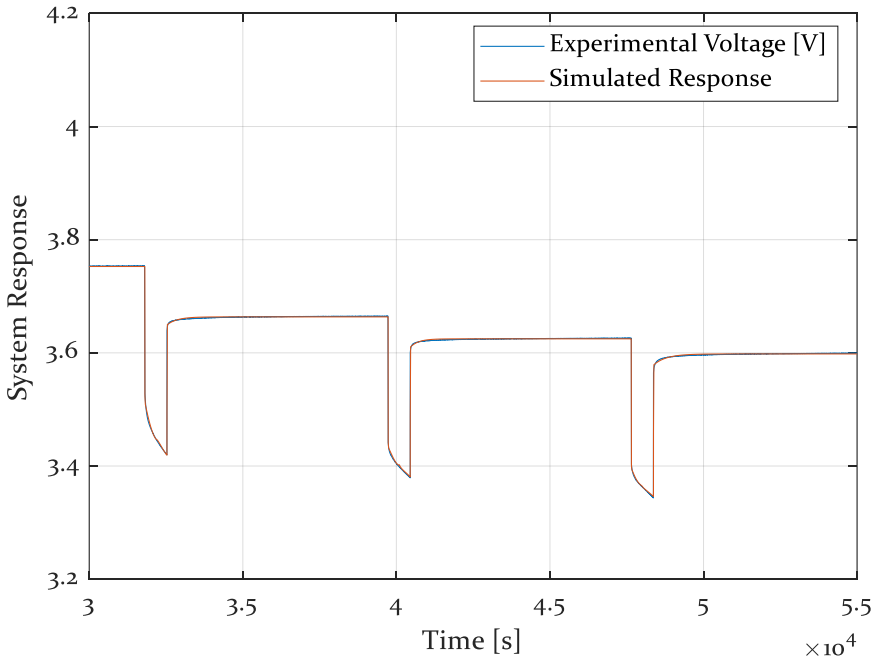

(b)

Figure 5.17: Samsung INR 18650 – 20R incremental OCV test results

Moreover, to validate the tuned parameters, the low current OCV test was utilized. The primary goal of the low current OCV test was to validate that the OCV of the battery corresponded to the measure terminal voltage. To do so, the battery was discharged at 0.1 A. Shown in Figure 5.18 is the OCV estimated by the signal V_{OCV} from the mechanical analogy battery model and the measured voltage.

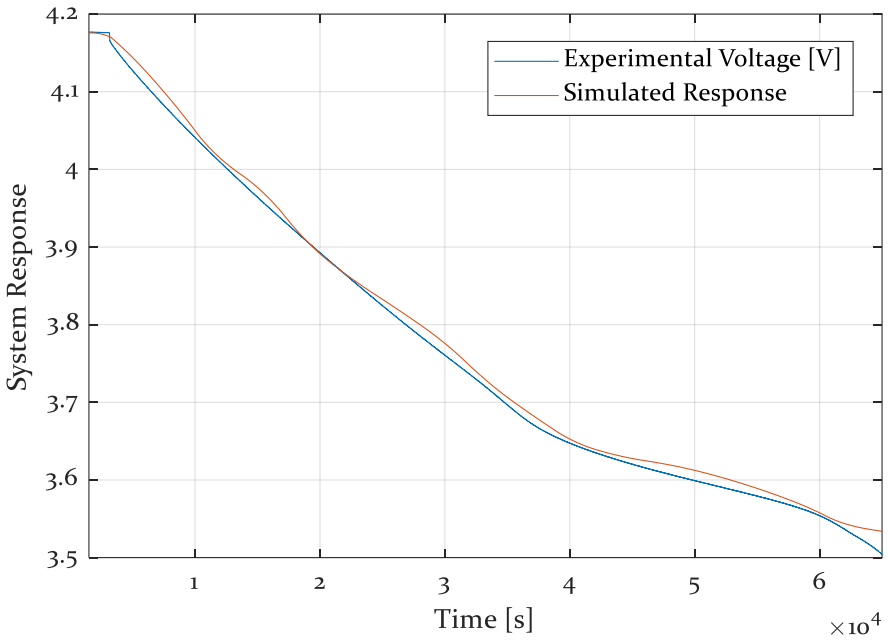

Figure 5.18: Samsung INR 18650 – 20R low current OCV test results

The simulated response of the model and the measured terminal voltage fit with a 0.26% standard deviation error; therefore, it can be deemed appropriate to validate the optimized parameters from the incremental current OCV test. The OCV predicted by the proposed model for both current profiles are in general agreement. Additionally, the OCV predicted by the model is in close agreement with that reported by Zhang *et al.* [22], which used the equivalent circuit model.

Chapter 6 Integration of the Battery Model with a BLDC Motor

6.1. Introduction

The main objective of the experiment conducted in this chapter is to evaluate the performance of the developed dynamic battery model in predicting the voltage response under dynamic loading from a real-life system.

A battery pack was constructed out of cylindrical cells to drive a benchtop BLDC motor with a magnetorheological brake as a programable load at varying running speeds. HPPC testing was carried out to calibrate the parameters of the mechanical analogy battery model as discussed in 3.1.2. The parameters of the model were then validated by examining the simulated voltage response of the model relative to the measured voltage of the pack to the current induced by the BLDC motor and the programmable load.

6.2. Experimental Methodologies

The battery used in this case is a Samsung 21700 – 40T [60]. The specification of the battery at a pack and cell level are demonstrated in Table 6.1.

Table 6.1: Battery pack specification

Parameter	Cell Level	Pack Level
Chemical system	LiNiMnCo /Graphite	
Form factor	Cylindrical - 27100	
Pack Configuration	6s1p	
Nominal capacity (mAh)	4000	
Maximum voltage (V)	4.2	25.2
Nominal voltage (V)	3.6	21.6
Cut-Off voltage (V)	2.5	15

Additionally, the NEO 202210 brushless DC motor [61] is used. The specifications of the motor are listed in Table 6.2.

Table 6.2: Motor specifications

Parameter	Variable
Nominal Voltage (V)	12
Empirical free speed (RPM)	5676
Empirical free running current (A)	1.8
Empirical stall current (A)	105
Empirical stall torque (Nm)	2.6
Empirical peak output power (W)	406
Mass (g)	425

Additionally, the magnetorheological brake used as a programmable load is MRB-2107-3 (LORD Co.) MR fluid brake. Table 6.3 gives the brake it's specifications [62].

Table 6.3: Magnetorheological brake specifications

Parameter	Variable
Diameter (mm)	92.2
Width (mm)	36.6
Weight (kg)	1.4
Maximum Torque (Nm)	7
Minimum Torque (Nm)	<0.34
Maximum Current (A)	1

Moreover, two Digit multi-meters (Keysight 34465A 6 ½) were utilized to measure the current and the voltage of the battery. The first multi-meter was connected in series to record current, whereas the second one was connected in parallel to measure the voltage response across the battery. To drive the control the motor and drive it, a SPARK Max motor controller was utilized. Figure 6.1 displays BLDC benchtop test rig.

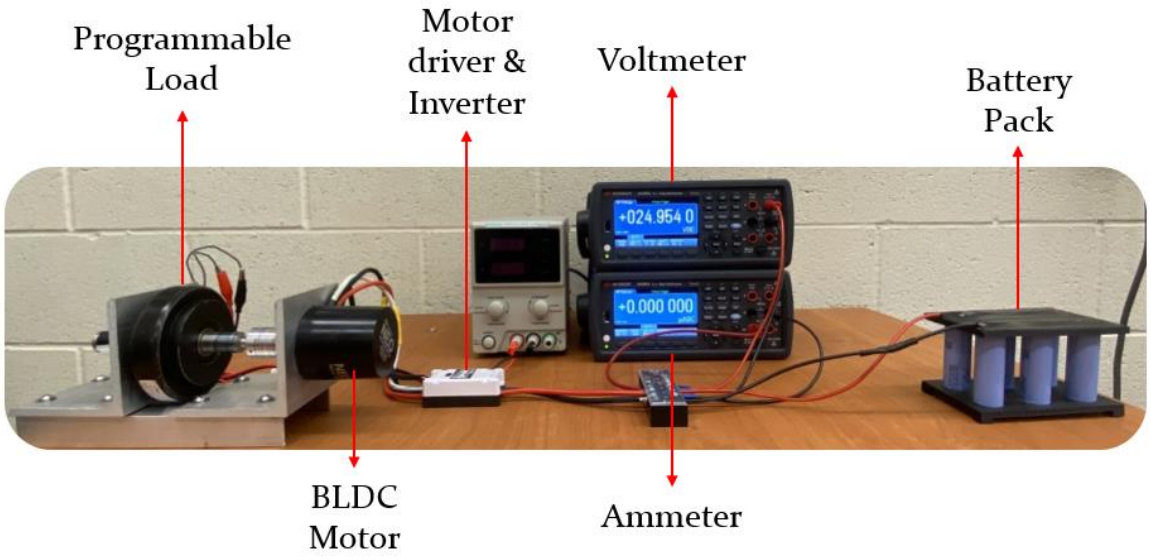

Figure 6.1: BLDC benchtop test rig

6.2.1. HPPC Testing

HPPC testing was conducted to determine the dynamic performance over the usable voltage ranges of the cell, which results in an accurate battery parameter identification to create robust model for simulation.

A similar testing circuit to the one shown in Figure 3.4 was constructed; however, a current probe (Keysight N2820A) to measure the current and a transistor was used to generate the current pulses driven by a waveform generator (Keysight 3360A). All the data was recorded and acquired utilizing a mixed signal oscilloscope (InifiniiVision MSOX4054A). Shown in Figure 6.2 is the experimental rig.

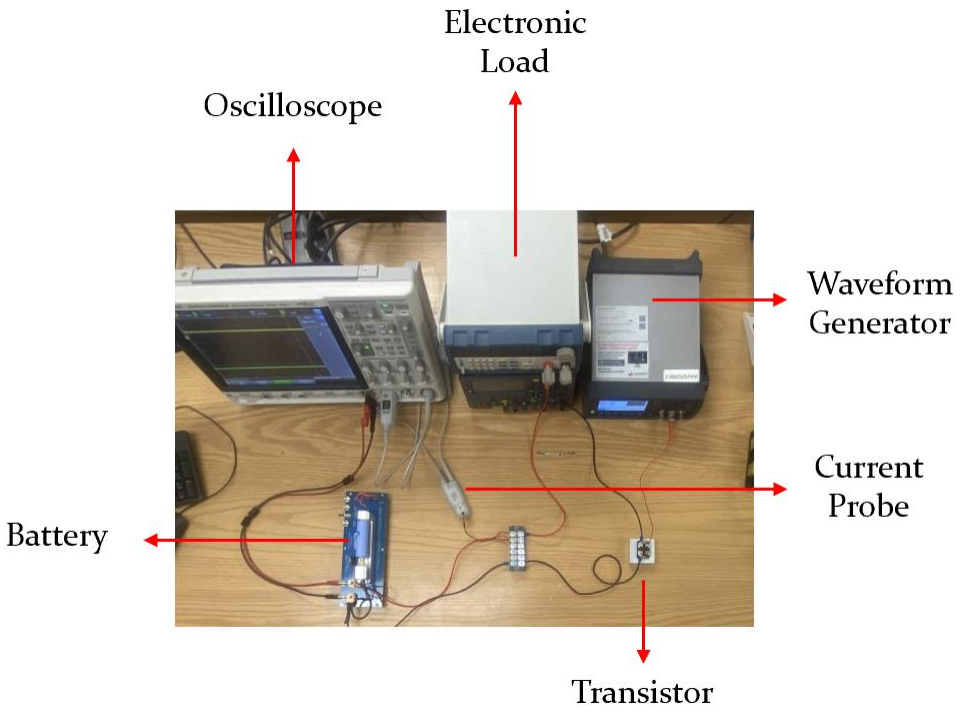

Figure 6.2: Samsung 21700-40T testing circuit

The battery was discharged at C/2 rate; therefore, at 2A and the test lasted roughly for four hours.

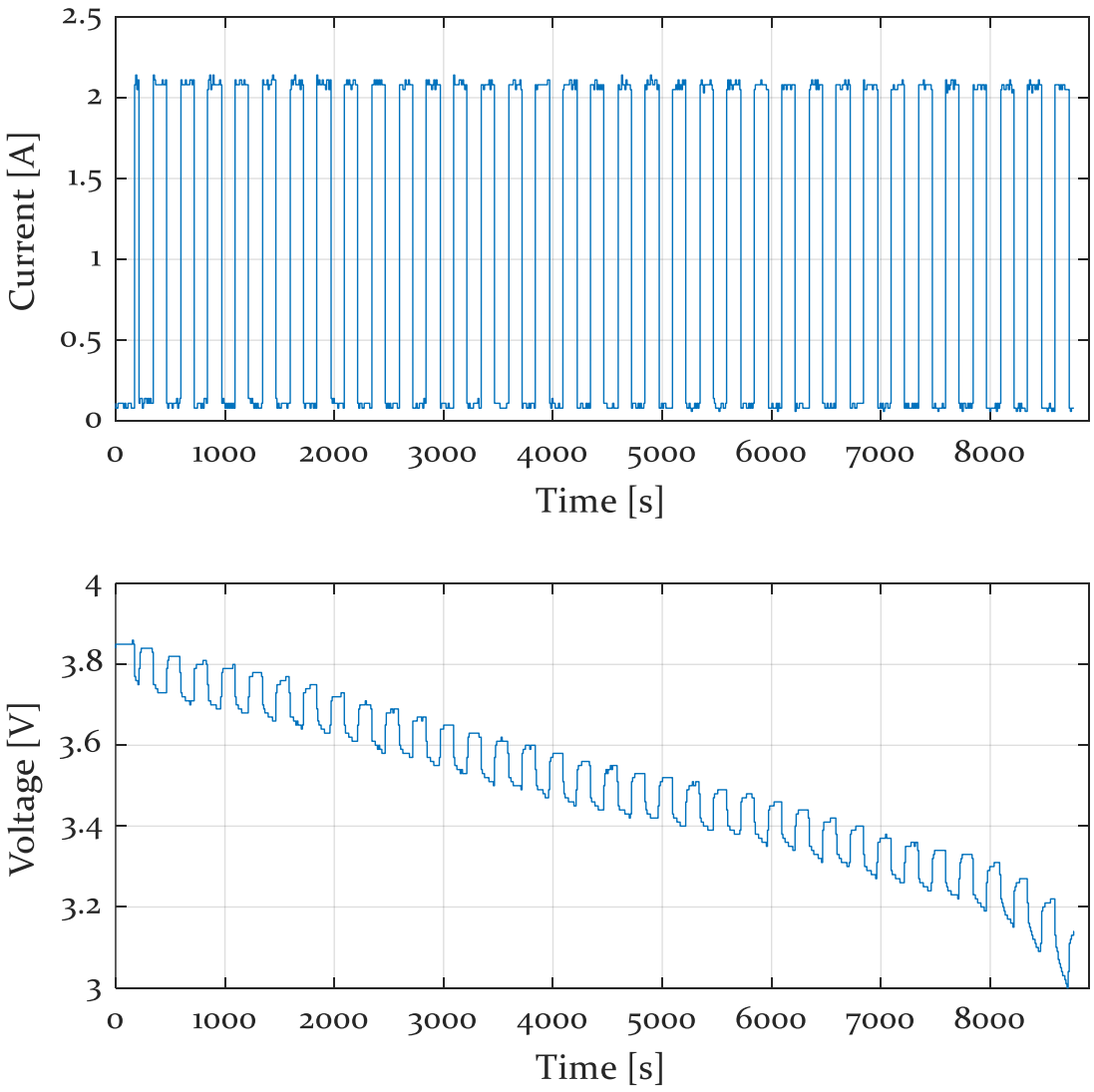

Figure 6.3: Samsung 27100 – 4OT HPPC testing data

6.2.2. BLDC Motor Cycling

Two cycles with varying speeds and loads were tested to obtain two different dynamic loads on the battery pack. The current on the magnetorheological brake was set to 0.01 A and 0.02 A for each test, respectively. Figure 6.4 illustrates the RPM, current load on the battery pack and voltage response the batteries for the tests.

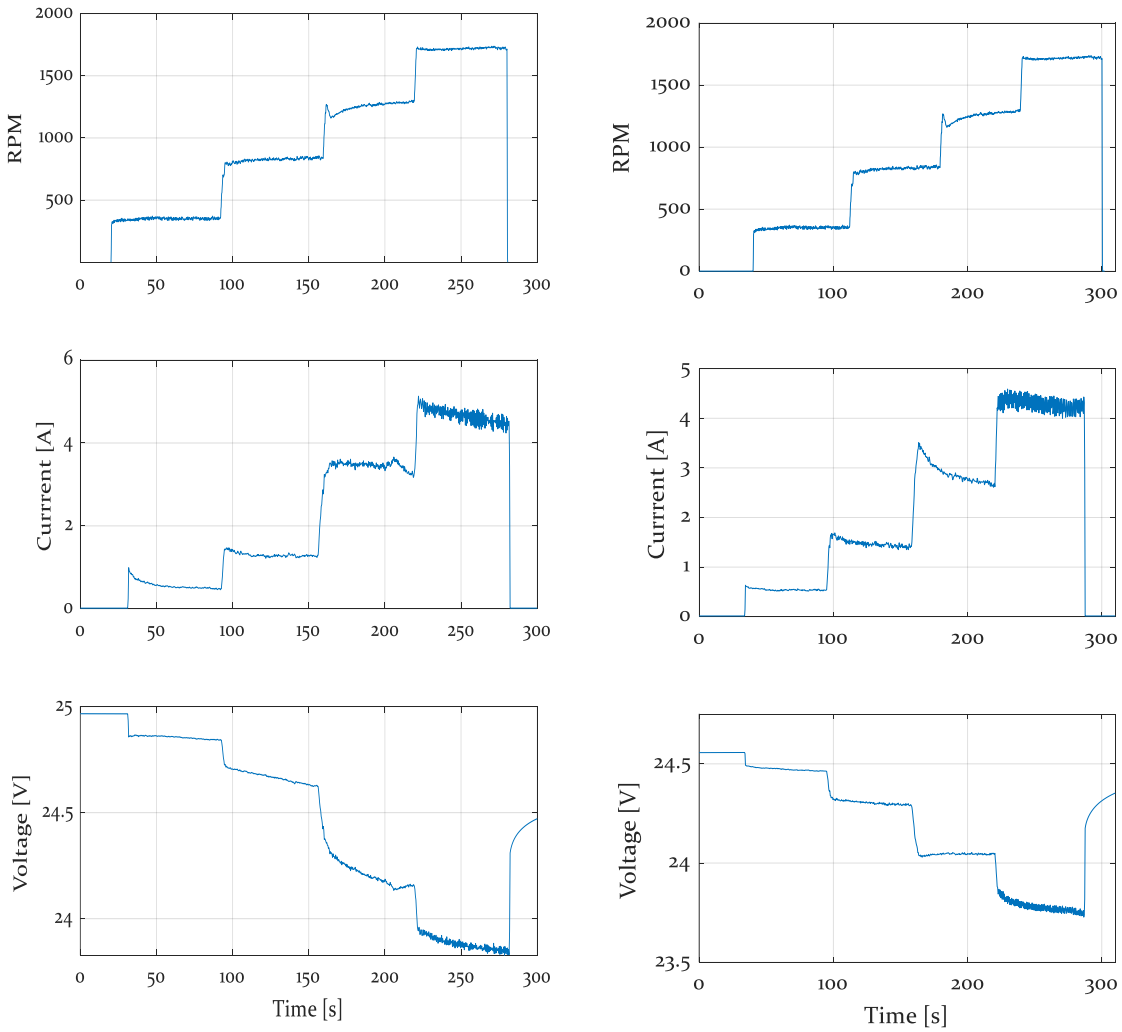

(a) (b)

Figure 6.4: BLDC cycling data

The second test was run after the first after allowing the battery to rest without charging. Additionally, the top plot shows the rotor speed which was increased every minute for each load test. With each increase in speed, there is an increase in current as the motor torque is needed to overcome the brake torque. Likewise, there are drops in the voltage of the battery due to the increase in current draw rates followed by a DC voltage decline.

6.3. Results & Discussion

The parameters of the mechanical analogy dynamic model were fitted to the experimental voltage following the HPPC test as shown in Figure 6.5. The model estimated the experimental voltage within 0.86% standard deviation of the error.

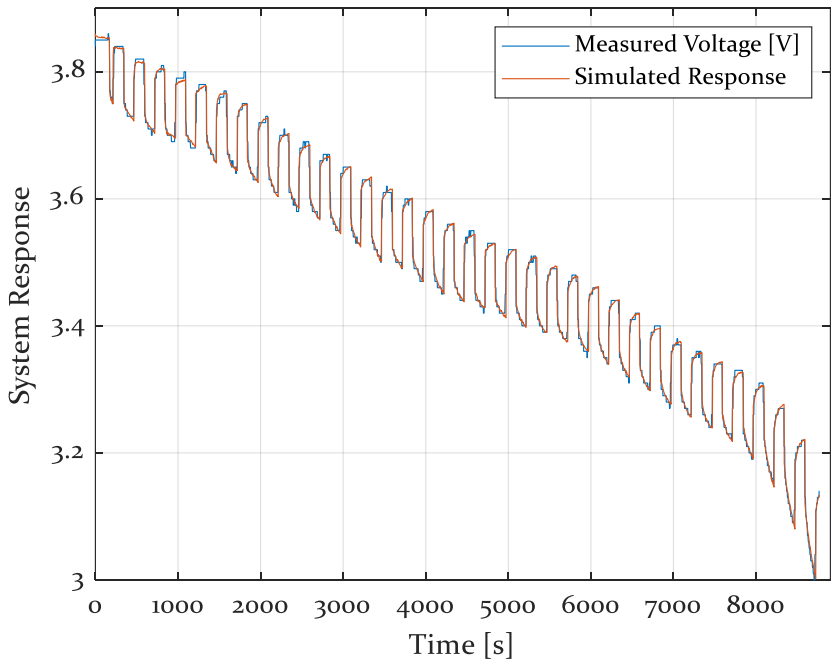

Figure 6.5: Samsung 27100-40T voltage response estimation

After the modal parameters were estimated and identified, they were utilized to estimate the voltage response of the BLDC cycles illustrated in Figure 6.4. Shown in Figure 6.6 are the estimated voltage response by the mechanical analogy dynamic model relative to that measured. The model fitted the measured data within 0.0385% and 0.0226% standard deviation of the error, for both load cycles, respectively.

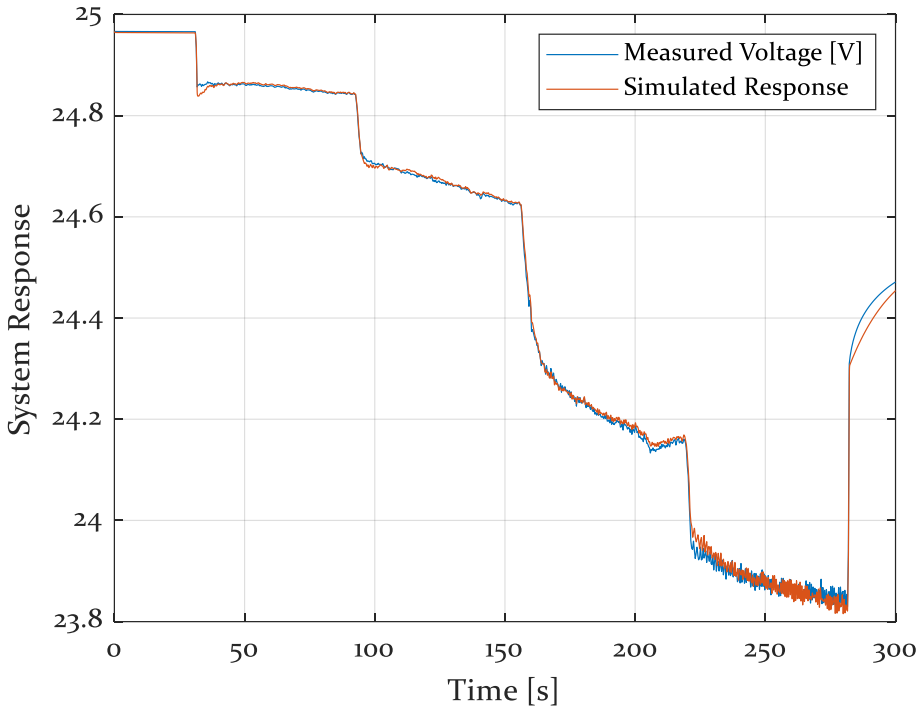

(a)

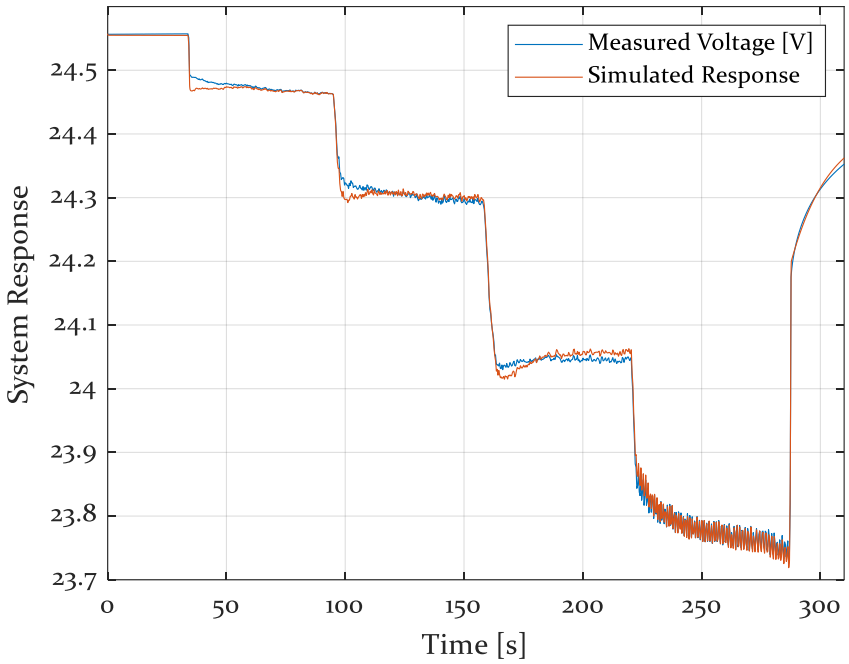

(b)

Figure 6.6: BLDC cycle estimated voltage response relative to measured data

Chapter 7 Conclusion

The study conducted in this paper proposed a novel mechanical analog to predict the nonlinear behavior of a battery in modal coordinates. The dynamics of the battery were predicted utilizing a three-degree-of-freedom, 6^{th} order spring-mass-damper system. The system was then decomposed into modal representation and considered as three independent single-degree-of-freedom modes to account for the discharge, mass transfer, and double-layer effects induced in the battery. The model parameters were tuned and optimized relative to the SOC to fit the response of the system to the experimental voltage measurements using a nonlinear least-squares method through the Trust-Region-Reflective algorithm. HPPC discharge experiments were conducted at two different discharge rates for each battery type. Current, voltage, and surface temperature were measured. The coupled dynamic model was able to predict the voltage and temperature responses within 2.15% and 0.40% standard deviation of the error. The temperature prediction method developed is a simple and intuitive coupled model that can be utilized to estimate the surface temperature of a battery in a dynamic setting. In addition, it can be used in the design process of a battery pack design. Furthermore, to validate the accuracy of the developed dynamic battery model, the model was utilized to estimate the dynamic current request load of a BLDC motor under varying speeds and loads. The

model estimated the voltage response of a battery pack within 0.0385% standard deviation of the error.

7.1. Future Work

To increase the accuracy of the voltage prediction, dynamic effects such as aging, electric, magnetic and cycling can be considered. Additionally, for a more precise surface temperature estimation, the entropic heating effects may be incorporated. For more complicated battery geometries, such as a pouch cell, the transient conduction two-dimensional model presented in 4.1.3 can be finalized and coupled with the mechanical analogy system to estimate the surface temperature and contours. Moreover, the model can be utilized to estimate the dynamics of the battery under various ambient temperatures and cycling conditions. Furthermore, the model can be integrated into more advanced simulation models such DC Microgrids or electrified vehicle powertrain.

Bibliography

[1] Y. Huang *et al.*, "Electrode Materials of Sodium-Ion Batteries toward Practical Application," *ACS Energy Lett*, vol. 3, no. 7, pp. 1604–1612, Jul. 2018, doi: 10.1021/acsenergylett.8b00609.

[2] M. A. Hannan, Md. M. Hoque, A. Hussain, Y. Yusof, and P. J. Ker, "State-of-the-Art and Energy Management System of Lithium-Ion Batteries in Electric Vehicle Applications: Issues and Recommendations," *IEEE Access*, vol. 6, pp. 19362–19378, 2018, doi: 10.1109/ACCESS.2018.2817655.

[3] N. O. Moraga, J. P. Xamán, and R. H. Araya, "Cooling Li-ion batteries of racing solar car by using multiple phase change materials," *Appl Therm Eng*, vol. 108, pp. 1041–1054, Sep. 2016, doi: 10.1016/j.applthermaleng.2016.07.183.

[4] M. v. Reddy, A. Mauger, C. M. Julien, A. Paolella, and K. Zaghib, "Brief History of Early Lithium-Battery Development," *Materials*, vol. 13, no. 8, p. 1884, Apr. 2020, doi: 10.3390/ma13081884.

[5] A. Masias, J. Marcicki, and W. A. Paxton, "Opportunities and Challenges of Lithium Ion Batteries in Automotive Applications," *ACS Energy Lett*, vol. 6, no. 2, pp. 621–630, Feb. 2021, doi: 10.1021/acsenergylett.0c02584.

[6] S. O'Dea, "Lithium-ion batteries - statistics & facts | Statista," *https://www.statista.com/topics/2049/lithium-ion-battery-industry/#topicOverview*.

[7] K. D. Stetzel, L. L. Aldrich, M. S. Trimboli, and G. L. Plett, "Electrochemical state and internal variables estimation using a reduced-order physics-based model of a lithium-ion cell and an extended Kalman filter," *J Power Sources*, vol. 278, pp. 490–505, Mar. 2015, doi: 10.1016/j.jpowsour.2014.11.135.

[8] G. Plett, *Battery Management Systems, Volume I: Battery Modeling*. Artech, 2015. [Online]. Available: http://ieeexplore.ieee.org/document/9100168

[9] *The Handbook of Lithium-Ion Battery Pack Design*. Elsevier, 2015. doi: 10.1016/C2013-0-23144-5.

[10] Y. Miao, P. Hynan, A. von Jouanne, and A. Yokochi, "Current Li-Ion Battery Technologies in Electric Vehicles and Opportunities for Advancements," *Energies (Basel)*, vol. 12, no. 6, p. 1074, Mar. 2019, doi: 10.3390/en12061074.

[11] R. Zhang *et al.*, "State of the Art of Lithium-Ion Battery SOC Estimation for Electrical Vehicles," *Energies (Basel)*, vol. 11, no. 7, p. 1820, Jul. 2018, doi: 10.3390/en11071820.

[12] A.J. Bard and L.R. Faulkner, *Electrochemical Methods: Fundamentals and Applications*, 2nd ed. New York: A John Wiley & Sons, Ltd., Publication, 2001.

[13] Christopher D. Rahn and Chao-Yang Wang, *Battery Systems Engineering*. A John Wiley & Sons, Ltd., Publication, 2013.

[14] A. Inc, "ANSYS Fluent Advanced Add-On Modules," *http://www.ansys.com* .

[15] K. H. Kwon, C. B. Shin, T. H. Kang, and C.-S. Kim, "A two-dimensional modeling of a lithium-polymer battery," *J Power Sources*, vol. 163, no. 1, pp. 151–157, Dec. 2006, doi: 10.1016/j.jpowsour.2006.03.012.

[16] M. Chen and G. A. Rincon-Mora, "Accurate electrical battery model capable of predicting runtime and I-V performance," *IEEE Transactions on Energy Conversion*, vol. 21, no. 2, pp. 504–511, Jun. 2006, doi: 10.1109/TEC.2006.874229.

[17] Y. Gao, C. Liu, S. Chen, X. Zhang, G. Fan, and C. Zhu, "Development and parameterization of a control-oriented electrochemical model of lithium-ion batteries for battery-management-systems applications," *Appl Energy*, vol. 309, p. 118521, Mar. 2022, doi: 10.1016/j.apenergy.2022.118521.

[18] F. Naseri, E. Schaltz, D.-I. Stroe, A. Gismero, and E. Farjah, "An Enhanced Equivalent Circuit Model With Real-Time Parameter Identification for Battery State-of-Charge Estimation," *IEEE Transactions on Industrial Electronics*, vol. 69, no. 4, pp. 3743–3751, Apr. 2022, doi: 10.1109/TIE.2021.3071679.

[19] Y. Liu, J. Li, G. Zhang, B. Hua, and N. Xiong, "State of Charge Estimation of Lithium-Ion Batteries Based on Temporal Convolutional Network and Transfer Learning," *IEEE Access*, vol. 9, pp. 34177–34187, 2021, doi: 10.1109/ACCESS.2021.3057371.

[20] X. Wu, X. Li, and J. Du, "State of Charge Estimation of Lithium-Ion Batteries Over Wide Temperature Range Using Unscented Kalman Filter," *IEEE Access*, vol. 6, pp. 41993–42003, 2018, doi: 10.1109/ACCESS.2018.2860050.

[21] X. Hua, C. Zhang, and G. Offer, "Finding a better fit for lithium ion batteries: A simple, novel, load dependent, modified equivalent circuit model and parameterization method," *J Power Sources*, vol. 484, p. 229117, Feb. 2021, doi: 10.1016/j.jpowsour.2020.229117.

[22] C. Zhang, W. Allafi, Q. Dinh, P. Ascencio, and J. Marco, "Online estimation of battery equivalent circuit model parameters and state of charge using decoupled least squares technique," *Energy*, vol. 142, pp. 678–688, Jan. 2018, doi: 10.1016/j.energy.2017.10.043.

[23] K. S. Hariharan and V. Senthil Kumar, "A nonlinear equivalent circuit model for lithium ion cells," *J Power Sources*, vol. 222, pp. 210–217, Jan. 2013, doi: 10.1016/j.jpowsour.2012.08.090.

[24] Z. Liu, X. Dang, and B. Jing, "A Novel Open Circuit Voltage Based State of Charge Estimation for Lithium-Ion Battery by Multi-Innovation Kalman Filter," *IEEE Access*, vol. 7, pp. 49432–49447, 2019, doi: 10.1109/ACCESS.2019.2910882.

[25] Z. Wei, C. Zou, F. Leng, B. H. Soong, and K.-J. Tseng, "Online Model Identification and State-of-Charge Estimate for Lithium-Ion Battery With a Recursive Total Least Squares-Based Observer," *IEEE Transactions on Industrial Electronics*, vol. 65, no. 2, pp. 1336–1346, Feb. 2018, doi: 10.1109/TIE.2017.2736480.

[26] Y. Li, Z. Wei, B. Xiong, and D. M. Vilathgamuwa, "Adaptive Ensemble-Based Electrochemical–Thermal Degradation State Estimation of Lithium-Ion Batteries," *IEEE Transactions on Industrial Electronics*, vol. 69, no. 7, pp. 6984–6996, Jul. 2022, doi: 10.1109/TIE.2021.3095815.

[27] J. Wu, Z. Wei, K. Liu, Z. Quan, and Y. Li, "Battery-Involved Energy Management for Hybrid Electric Bus Based on Expert-Assistance Deep Deterministic Policy Gradient Algorithm," *IEEE Trans Veh Technol*, vol. 69, no. 11, pp. 12786–12796, Nov. 2020, doi: 10.1109/TVT.2020.3025627.

[28] M. Paschero, G. L. Storti, A. Rizzi, F. M. F. Mascioli, and G. Rizzoni, "A Novel Mechanical Analogy-Based Battery Model for SoC Estimation Using a Multicell EKF," *IEEE Trans Sustain Energy*, vol. 7, no. 4, pp. 1695–1702, Oct. 2016, doi: 10.1109/TSTE.2016.2574755.

[29] Z. Wei, S. Meng, B. Xiong, D. Ji, and K. J. Tseng, "Enhanced online model identification and state of charge estimation for lithium-ion battery with a FBCRLS based observer," *Appl Energy*, vol. 181, pp. 332–341, Nov. 2016, doi: 10.1016/j.apenergy.2016.08.103.

[30] F. Zheng, Y. Xing, J. Jiang, B. Sun, J. Kim, and M. Pecht, "Influence of different open circuit voltage tests on state of charge online estimation for lithium-ion batteries," *Appl Energy*, vol. 183, pp. 513–525, Dec. 2016, doi: 10.1016/j.apenergy.2016.09.010.

[31] J. Hu, H. He, Z. Wei, and Y. Li, "Disturbance-Immune and Aging-Robust Internal Short Circuit Diagnostic for Lithium-Ion Battery," *IEEE Transactions on Industrial Electronics*, vol. 69, no. 2, pp. 1988–1999, Feb. 2022, doi: 10.1109/TIE.2021.3063968.

[32] C. She, L. Zhang, Z. Wang, F. Sun, P. Liu, and C. Song, "Battery State of Health Estimation Based on Incremental Capacity Analysis Method: Synthesizing from Cell-Level Test to Real-World Application," *IEEE J Emerg Sel Top Power Electron*, pp. 1–1, 2022, doi: 10.1109/JESTPE.2021.3112754.

[33] Z. Wang, C. Song, L. Zhang, Y. Zhao, P. Liu, and D. G. Dorrell, "A Data-Driven Method for Battery Charging Capacity Abnormality Diagnosis in Electric Vehicle Applications," *IEEE Transactions on Transportation Electrification*, vol. 8, no. 1, pp. 990–999, Mar. 2022, doi: 10.1109/TTE.2021.3117841.

[34] X. Hu, H. Yuan, C. Zou, Z. Li, and L. Zhang, "Co-Estimation of State of Charge and State of Health for Lithium-Ion Batteries Based on Fractional-Order Calculus," *IEEE Trans Veh Technol*, vol. 67, no. 11, pp. 10319–10329, Nov. 2018, doi: 10.1109/TVT.2018.2865664.

[35] J. Zhang, L. Zhang, F. Sun, and Z. Wang, "An Overview on Thermal Safety Issues of Lithium-ion Batteries for Electric Vehicle Application," *IEEE Access*, vol. 6, pp. 23848–23863, 2018, doi: 10.1109/ACCESS.2018.2824838.

[36] T. Mesbahi, R. B. Sugrañes, R. Bakri, and P. Bartholomeüs, "Coupled electro-thermal modeling of lithium-ion batteries for electric vehicle application," *J Energy Storage*, vol. 35, p. 102260, Mar. 2021, doi: 10.1016/j.est.2021.102260.

[37] H. Ruan *et al.*, "A modified-electrochemical impedance spectroscopy-based multi-time-scale fractional-order model for lithium-ion batteries," *Electrochim Acta*, vol. 394, p. 139066, Oct. 2021, doi: 10.1016/j.electacta.2021.139066.

[38] J. Chiew, C. S. Chin, W. D. Toh, Z. Gao, J. Jia, and CZ. Zhang, "A pseudo three-dimensional electrochemical-thermal model of a cylindrical LiFePO4/graphite battery," *Appl Therm Eng*, vol. 147, pp. 450–463, Jan. 2019, doi: 10.1016/j.applthermaleng.2018.10.108.

[39] R. Mahamud and C. Park, "Reciprocating air flow for Li-ion battery thermal management to improve temperature uniformity," *J Power Sources*, vol. 196, no. 13, pp. 5685–5696, Jul. 2011, doi: 10.1016/j.jpowsour.2011.02.076.

[40] X. Zhang, "Thermal analysis of a cylindrical lithium-ion battery," *Electrochim Acta*, vol. 56, no. 3, pp. 1246–1255, Jan. 2011, doi: 10.1016/j.electacta.2010.10.054.

[41] S. Panchal, I. Dincer, M. Agelin-Chaab, R. Fraser, and M. Fowler, "Experimental and theoretical investigation of temperature distributions in a prismatic lithium-ion battery," *International Journal of Thermal Sciences*, vol. 99, pp. 204–212, Jan. 2016, doi: 10.1016/j.ijthermalsci.2015.08.016.

[42] Y. Ye, Y. Shi, and A. A. O. Tay, "Electro-thermal cycle life model for lithium iron phosphate battery," *J Power Sources*, vol. 217, pp. 509–518, Nov. 2012, doi: 10.1016/j.jpowsour.2012.06.055.

[43] W. Huang, W. Zhang, A. Chen, Y. Zhang, and M. Li, "A Co-Simulation Method Based on Coupled Thermoelectric Model for Electrical and Thermal Behavior of the Lithium-ion Battery," *IEEE Access*, vol. 7, pp. 180727–180737, 2019, doi: 10.1109/ACCESS.2019.2958940.

[44] Z. Wang, J. Ma, and L. Zhang, "Finite Element Thermal Model and Simulation for a Cylindrical Li-Ion Battery," *IEEE Access*, vol. 5, pp. 15372–15379, 2017, doi: 10.1109/ACCESS.2017.2723436.

[45] Y. Li, Z. Wei, B. Xiong, and D. M. Vilathgamuwa, "Adaptive Ensemble-Based Electrochemical–Thermal Degradation State Estimation of Lithium-Ion Batteries," *IEEE Transactions on Industrial Electronics*, vol. 69, no. 7, pp. 6984–6996, Jul. 2022, doi: 10.1109/TIE.2021.3095815.

[46] Jon P. Christopherson, "Battery Test Manual For Electric Vehicles ," 2015.

[47] M. Messing, "ADVANCED CHARACTERIZATION OF BATTERY CELL DYNAMICS," PhD Dissertation , McMaster University , 2021.

[48] "Panasonic Tesla Model 3, Batemo Cell Library," *https://www.batemo.de/products/batemo-cell-library/tesla-model-3/*. .

[49] "Samsung INR18650-25R, Energy Business Division," *https://www.powerstream.com/p/INR18650-25R-datasheet.pdf*.

[50] "2013 Chevrolet Volt – VIN 3929 Advanced Vehicle Testing – Beginning-of-Test Battery Testing Results," *https://www.energy.gov/sites/prod/files/2014/02/f7/battery_volt_3929.pdf*.

[51] "Center for Advanced Life Cycle Engineering "Battery Research Data.," *https://calce.umd.edu/data#INR*.

[52] "Samsung, 'Specifications of Product: Lithium-ion rechargeable cell for power tools,' INR18650-20R."

[53] K. I. Alsharif *et al.*, "A Novel Modal Representation of Battery Dynamics," *IEEE Access*, vol. 10, pp. 16793–16806, 2022, doi: 10.1109/ACCESS.2022.3149617.

[54] K. I. Alsharif *et al.*, "A Coupled Thermo-Mechanical Dynamic Characterization of Cylindrical Batteries," *IEEE Access*, vol. 10, pp. 51708–51722, 2022, doi: 10.1109/ACCESS.2022.3173640.

[55] D.J. Inman, *Engineering Vibrations*, 2nd ed. Upper Saddle River, NY, USA: Prentice Hall, 2001.

[56] Y.A. Çengel and A.J. Ghajar, *Heat and Mass Transfer and Applications*, 5th ed. Penn Plaza, NY, USA, 2015.

[57] D. Bernardi, E. Pawlikowski, and J. Newman, "A General Energy Balance for Battery Systems," *J Electrochem Soc*, vol. 132, no. 1, pp. 5–12, Jan. 1985, doi: 10.1149/1.2113792.

[58] X. Lin *et al.*, "A lumped-parameter electro-thermal model for cylindrical batteries," *J Power Sources*, vol. 257, pp. 1–11, Jul. 2014, doi: 10.1016/j.jpowsour.2014.01.097.

[59] A. Jossen, "Fundamentals of battery dynamics," *J Power Sources*, vol. 154, no. 2, pp. 530–538, Mar. 2006, doi: 10.1016/j.jpowsour.2005.10.041.

[60] "Samsung 40T 21700 4000mAh 35A Battery - INR21700-40T (40T3)," *https://cdn.shopify.com/s/files/1/0481/9678/0183/files/Samsung_Introduction_of_New_40T_v3.pdf?v=1612843210*.

[61] "NEO Brushless Motor V1.1," *https://www.revrobotics.com/rev-21-1650/*.

[62] H. Tomori, S. Nagai, T. Majima, and T. Nakamura, "Variable impedance control with an artificial muscle manipulator using instantaneous force and MR brake," in *2013 IEEE/RSJ International Conference on Intelligent Robots and Systems*, Nov. 2013, pp. 5396–5403. doi: 10.1109/IROS.2013.6697137.